

TOI-4552 b: A new ultra-short period rocky world revealed by NIRPS and TESS

Avidaan Srivastava^{1,*}, René Doyon^{1,2}, François Bouchy³, Étienne Artigau^{1,2}, Charles Cadieux¹, Nicole Gromek⁴, Elisa Delgado-Mena^{5,6}, Yuri S. Messias^{1,7}, Xavier Bonfils⁸, Roseane de Lima Gomes^{1,7}, Susana C. C. Barros^{6,9}, Björn Benneke^{10,1}, Marta Bryan¹¹, Ryan Cloutier⁴, Nicolas B. Cowan^{12,13}, Eduardo Cristo⁶, Xavier Delfosse⁸, Xavier Dumusque³, David Ehrenreich^{3,14}, Jonay I. González Hernández^{15,16}, David Lafrenière¹, Izan de Castro Leão⁷, Christophe Lovis³, Alejandro Suárez Mascareño^{15,16}, Bruno L. Canto Martins⁷, Jose Renan De Medeiros⁷, Lucile Mignon^{3,8}, Christoph Mordasini¹⁷, Francesco Pepe³, Rafael Rebolo^{15,16,18}, Jason Rowe¹⁹, Nuno C. Santos^{6,9}, Damien Ségransan³, Stéphane Udry³, Diana Valencia¹¹, Gregg Wade^{20,21}, Jose Manuel Almenara⁸, Karen A. Collins²², Dennis M. Conti²³, George Dransfield²⁴, Elsa Ducrot^{25,26}, Zahra Essack²⁷, Dasaev O. Fontinele⁷, Thierry Forveille⁸, Marziye Jafariyazani²⁸, Pierrot Lamontagne¹, Alexandrine L'Heureux¹, Khaled Al Moulla^{6,3}, Ares Osborn^{8,4,29}, Léna Parc³, David R. Rodriguez³⁰, Richard P. Schwartz²², Madison G. Scott³¹, Avi Shporer³², Atanas K. Stefanov^{15,16}, Mathilde Timmermans^{31,33}, Amaury H.M.J. Triaud³¹, Joost P. Wardenier^{17,1}, Drew Weisserman⁴, Sebastián Zúñiga-Fernández³³

(Affiliations can be found after the references)

Received December 23, 2025; accepted March 16, 2025

ABSTRACT

Context. A particularly intriguing subclass of rocky exoplanets are the ultra-short period (USP) worlds that orbit their host stars in less than a day. These planets are particularly rare around M dwarf stars, with so far only ten that have a constrained mass and radius.

Aims. We present the validation and characterization of the ultra-short period (0.3 days), Earth-sized planet TOI-4552 b orbiting a nearby (27.26-pc away) M4.5V dwarf.

Methods. Complementing the TESS photometry, ground-based transit observations from LCO, ExTrA and SPECULOOS validated the planetary radius and cleared the field of any contaminants. Speckle imaging with Zorro (Gemini-S) rules out false positive scenarios caused by eclipsing binary sources. Spectroscopic observations with NIRPS and HARPS were used to obtain stellar abundances, constrain the planetary mass, and, in conjunction with the transit observations, estimate the orbital parameters.

Results. TOI-4552 is a quiet star exhibiting no short-term stellar variations seen in photometric or radial velocity data that can be associated to stellar rotation. Long-term photometric data from ASAS-SN also suggests a lack of activity signals. TOI-4552 b ($M_p = 1.83 \pm 0.47 M_\oplus$, $R_p = 1.11 \pm 0.04 R_\oplus$) lies between the Earth-like and iron-rich composition tracks on the Mass-Radius diagram. The exoplanet interior structure model, without constraints from refractory abundance ratio, yields a core mass fraction (CMF) of $0.54^{+0.17}_{-0.25}$ and a bulk density of 7.74 g/cm^3 . Since the CMF spans a wide range due to the large uncertainty on the mass, the definitive interior composition cannot be determined with the current dataset.

Conclusions. TOI-4552 b hints as being marginally more iron-rich compared to the Earth but confirmation of its status requires additional, precise radial velocity measurements. Combined with its high emission spectroscopic metric (ESM = 19.5), negligible stellar activity and short orbital period, TOI-4552 b emerges as a compelling target for atmospheric and surface composition studies with JWST.

Key words. near-infrared spectroscopy – exoplanets – ultra-short period – core mass fraction

1. Introduction

The Transiting Exoplanet Survey Satellite (TESS; Ricker et al. 2015) mission has been at the forefront of discovering new worlds in the solar neighbourhood via the transit method. As of 2025, more than 7000 planetary candidates have been flagged in TESS datasets around a varied population of stars. These stars include the M dwarfs, cooler ($T_{\text{eff}} < 4000 \text{ K}$) and less massive ($M_* = 0.1 - 0.7 M_\odot$) than the Sun but more numerous in our galaxy (e.g., Chabrier 2001; Bochanski et al. 2010). Their smaller size facilitates larger signals for transiting planets and their low mass allows for the detection of smaller planets around them. All these factors make exoplanets easier to detect around such stars, which are also known to host a large population of

rocky planets (Bonfils et al. 2013; Dressing & Charbonneau 2015; Gillis et al. 2026). However, it is important to note that many M dwarfs exhibit substantial stellar activity (e.g., Galletta et al. 2025; Rajpurohit et al. 2025; Mignon et al. 2023; Roettenbacher & Kane 2017), which can significantly hinder planet detection. As a result, while M dwarfs offer clear advantages for exoplanet searches, their intrinsic activity can also present notable observational challenges.

Due to their lower effective temperatures, M-type stars are brighter in the near infrared (NIR) as opposed to the visible (VIS) wavelength band. To extract the maximum amount of spectral information from these stars, a new state-of-the-art instrument, Near Infra-Red Planet Searcher (NIRPS, Bouchy et al. 2025, 2017), has been developed. NIRPS is installed on the 3.6-

m telescope at La Silla Observatory in Chile and works alongside HARPS (Mayor et al. 2003). As part of the Guaranteed Time Observations (GTO) sub-programme 2 (SP2) of NIRPS, we follow up TESS transiting candidates to confirm planetary detections and measure their masses. Measurement of both the mass and radius of a planet is crucial to place meaningful constraints on its interior and atmospheric composition through the bulk density.

One particularly interesting subclass of rocky planets are the ultra-short period (USP) worlds, uniquely identified by their orbital period of less than 1 day. While some, such as 55 Cancri e (Dawson & Fabrycky 2010; McArthur et al. 2004), have been studied extensively, their rarity makes it difficult to conduct a wider study. Only 10 USPs orbiting M dwarfs have published masses and radii (Lee et al. 2025; Dai et al. 2024; Murgas et al. 2024; Burt et al. 2024; Palle et al. 2023; Essack et al. 2023; Lam et al. 2021; Bluhm et al. 2021; Cloutier et al. 2021; Hirano et al. 2021; Cloutier et al. 2020; Shporer et al. 2020). Such a small dataset is not enough to develop a complete understanding about the nature of these worlds. James Webb Space Telescope (JWST; Gardner et al. 2006, 2023) observations have revealed that several USPs are barren worlds lacking substantial atmospheres (e.g., Kreidberg et al. 2019; Luque et al. 2025), likely stripped by the intense stellar irradiation they endure ($> 200 S_{\oplus}$). As a result, interior structure models can be run without atmospheric degeneracies. Since previous studies (Plotnikov & Valencia 2020; Brinkman et al. 2024) have concluded that rocky planets exhibit a diverse range of compositions, it is only by expanding the sample size that we can identify any trends and conduct population studies.

Beyond their compositional significance, USPs offer unique opportunities for surface geological studies with JWST. Their short orbital periods make them amenable to short and repeated observations, and their high irradiation can drive detectable phase-curve signals. Phase-curve and secondary eclipse measurements can constrain albedos, day–night temperature contrasts, and even surface mineralogy in the absence of an atmosphere (e.g., Hu et al. 2012; Paragas et al. 2025).

We present the discovery and characterization of a USP, TOI-4552 b, as part of the NIRPS GTO SP2. The article is structured as follows: Section 2 discusses the various facilities (TESS, ExTrA, SPECULOOS, LCO, Zorro, HARPS+NIRPS), both space- and ground-based, used to observe the target star and construct our dataset. Section 3 covers the various methods used to characterize the star using photometry and HARPS+NIRPS spectroscopy. In Section 4 we present our global photometry and RV model and analysis of the results. Section 5 dives deeper into the results and discusses the interior structure modelling and future scientific relevance of TOI-4552 b. Finally, in Section 6 we summarise the article and present its conclusions.

2. Observations

2.1. TESS photometry

TOI-4552 b (TIC 248250955) was first alerted as a Level 1 planetary candidate (Guerrero et al. 2021) on October 28, 2021 by the TESS Science Processing Operations Center (SPOC, Jenkins et al. 2016) pipeline at NASA Ames Research Centre on the publicly available TESS data webpage¹. It has been observed in TESS sectors 12 (year 1), 39 (year 3) and 66 (year 5), each with a 120-second exposure time as well as a 20-second exposure time

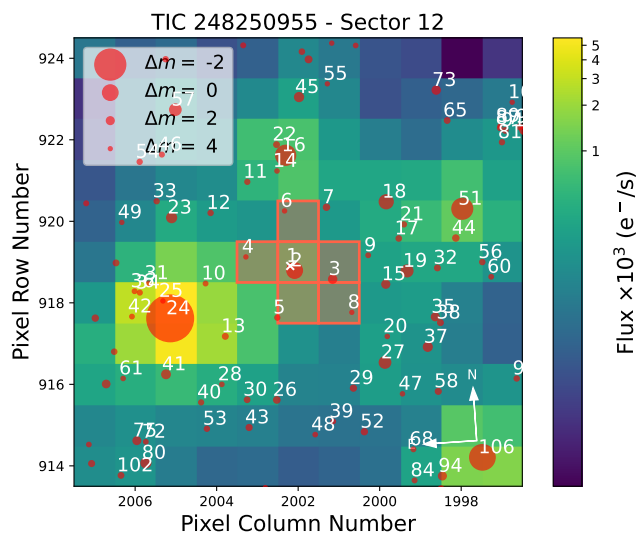


Fig. 1: Target pixel file (TPF) of TOI-4552 for TESS sector 12, created using `tpfplotter` (Aller et al. 2020). The pixels ($21''$ pixel scale) outlined in orange correspond to the aperture mask used to extract the SAP flux for the lightcurve. All Gaia DR3 (Gaia Collaboration et al. 2023) sources in the field are numbered, with “1” marking TOI-4552. The size of the red circles is representative of the TESS magnitude of the stars relative to TOI-4552. Since it is a crowded field, TESS SPOC provides lightcurves corrected for the dilution caused by the strongest contaminants. Fig. A.1 shows the TPF of all three sectors with the primary contaminants.

for sector 66. The target was imaged on CCD 2 of camera 1 for all three sectors. Owing to the short orbital period of 0.3011 days, each sector contains approximately 70 transits.

Since the TESS pixels are relatively large ($21''$ on sky), the retrieved stellar flux of its targets are often contaminated by a neighbour. `tpfplotter` (Aller et al. 2020) was used to plot the target pixel file (TPF) for Sector 12 (Fig. 1) consisting of neighbouring sources from the Gaia DR3 (Gaia Collaboration et al. 2023). The TPF highlights the pixels used for the aperture mask to obtain the Simple Aperture Photometry (SAP; Twicken et al. 2010; Morris et al. 2020) flux in orange. Due to the crowded field, we used TESS-cont (Castro-González et al. 2024) to identify the strongest sources of contamination. These stars in along with their angular separation from TOI-4552 and relative percentage of contamination are: TIC 248250924 ($63''$; 17%), TIC 248250937 ($18''$; 7%), TIC 248251013 ($58''$; 2%), TIC 248250948 ($4''$; 1.2%) and TIC 248250933 ($44''$; 1%). The TPF for all three sectors highlighting these contaminants are presented in Fig. A.1.

As per the Data Validation Report (DVR; Twicken et al. 2018) produced on October 30, 2023, which presents a joint analysis of the target for all three sectors, the lightcurves were corrected for dilution and crowding effected by a factor in agreement with the aforementioned sources. Additionally, the Centroid Test and Eclipsing Binary Discrimination Test were conducted for validation and ruled in favour of TOI-4552 as the host of the planetary candidate. A Signal-to-Noise ratio (SNR) of 11.8 was reported in the DVR for the fit, denoting that the candidate is likely a planet ($\text{SNR} > 10$). Our analysis uses the normalised Presearch Data Conditioning Simple Aperture Photometry (PDCSAP; Smith et al. 2012; Stumpe et al. 2012, 2014) flux which was corrected for dilution in the TESS aperture by known contaminating sources as well as for instrumental systematics. Fig. 2 showcases the three TESS sectors phase

¹ <https://tev.mit.edu/>

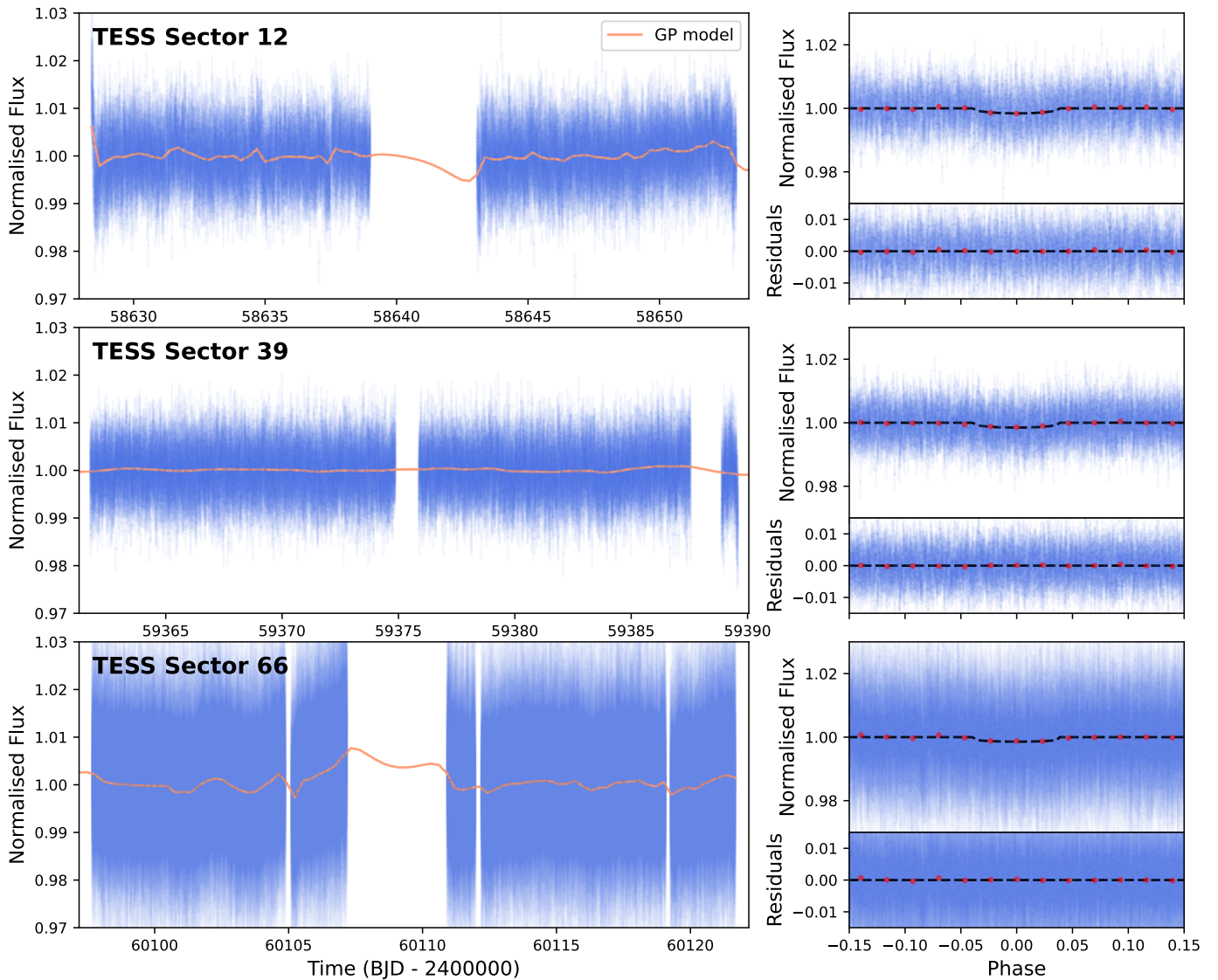


Fig. 2: TESS transit lightcurves from sectors 12, 39 and 66. The normalised flux (blue points) as well as the gaussian process (GP) model (orange) used to detrend the lightcurve is plotted on the left. The phase-folded lightcurves centred on the transit of TOI-4552 b, transit model (black dashed line), binned flux (red points) and the residuals after fitting for the transit are plotted on the right, for each sector. Sectors 12 and 39 were observed by TESS at a 2 minute cadence, whereas Sector 66 was observed at a 20 second cadence. Since TOI-4552 b is a USP, we choose to keep the high cadence of Sector 66 to provide a better sampling at the expense of lower precision.

folded at the period and time of conjunction of TOI-4552 b.

The large $21''$ pixel scale of TESS can also create some ambiguity regarding which star is hosting the transiting planet candidate if multiple stars are located inside the aperture mask. Since the TESS pixel centred on TOI-4552 shows at least one apparent Gaia-detected contaminant, follow-up with seeing-limited ground-based photometry ($\sim 1\text{--}2''$) and diffraction-limited high-angular-resolution imaging is required to attribute the transit event to the correct star and vet false positives from other eclipsing binaries in the aperture mask. Several facilities around the world contribute to this effort under the TESS Follow-up Observing program (TFOP²) Working Group Sub-Group 1 (SG1; Collins 2019).

² <https://tess.mit.edu/followup/>

2.2. Ground-based transit confirmations: ExTrA

ExTrA (Bonfils et al. 2015) is a near-infrared (0.85 to $1.55 \mu\text{m}$), multi-object spectrograph fed by three F/8 telescopes each with 60 cm primary mirrors. We used ExTrA to intensely monitor TOI-4552 from 2022 to 2024 over twenty-six individual nights as part of TFOP SG1 using the low resolution ($R\sim 20$) mode. On nine of those nights, all three telescopes observed the transit, two telescopes observed the transit on sixteen nights and for one night only one telescope observed the transit totalling 61 full/partial transits used in our analysis (Fig. A.2). The data reduction and detrending was performed using the methodology described in Cointepas et al. (2021). The closest contaminant star, TIC 248250948, lies $3.94''$ from the target, so we adopted a $3.86''$ aperture to minimise dilution. The typical seeing during the observations was about $1.3''$, which ensured that most of the stellar flux remained within the chosen aperture. A 1.2% dilution correction was then applied during the lightcurve extraction

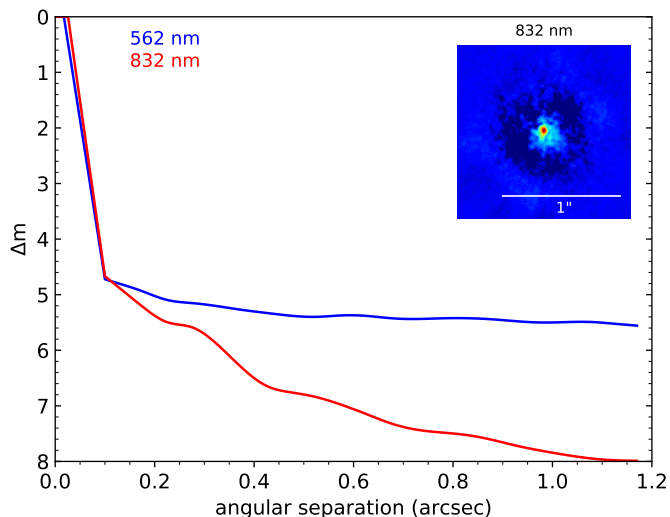


Fig. 3: High contrast image of TOI-4552 using Zorro at Gemini-S (Scott et al. 2021; Howell et al. 2025) in the two simultaneous channels (562-nm and 832-nm) as a function of on-sky separation. Four nights of observations were combined here. The $5\text{-}\sigma$ contrast curve shows no evidence for neighbours or companions contaminating the signal.

and detrending level to remove any residual contamination from nearby sources.

2.3. Ground-based transit confirmations: LCOGT

The Las Cumbres Observatory Global Telescope Network (LCOGT; Brown et al. 2013) is composed of robotic 1.0 m class telescopes distributed across multiple observatories worldwide and is regularly used for TFOP SG1 follow-up. As part of this program, TOI-4552 was monitored in 2022, yielding four full transits from the Cerro Tololo Inter-American Observatory (CTIO, Chile) and two full transits from the South African Astronomical Observatory (SAAO, South Africa), all in the Sloan- i' photometric bandpass. All data were calibrated using the standard BANZAI pipeline (McCully et al. 2018) and differential photometric data were extracted using AstroImageJ (Collins et al. 2017). The typical photometric aperture radius for all observations was $2.7''$. Fig. A.2 shows the detrended, combined, and phase-folded transit lightcurves used in our joint analysis.

2.4. Ground-based transit confirmations: SPECULOOS

The Search for habitable Planets Eclipsing ULtra-cOOl Stars (SPECULOOS; Delrez et al. 2018) southern observatory consists of four robotic 1.0 m telescopes (Europa, Ganymede, Io, Callisto) located at the European Southern Observatory (ESO) Paranal site, suitable for transit observations of late M-type stars such as TOI-4552. Thirteen transits were recorded from 2022 to 2024 with the Ganymede, Europa and Io telescopes in various combination of the Sloan- g' , r' and z' filters totalling 20 individual transits used in our analysis. The `allesfitter` python package (Günther & Daylan 2021) was used to detrend the transit lightcurves (Fig. A.2) following the procedure similar to Dransfield et al. 2024 and Henderson et al. 2024.

2.5. High resolution imaging: Zorro

There may exist additional gravitationally bound or unbound sources, unresolved in Gaia DR3, that may contaminate the derived planetary and stellar parameters. To assess the impact of such sources (if any) and further rule out false positive scenarios, as is the standard procedure for TESS objects of interest (TOIs), we observed TOI-4552 with the Zorro imager (Scott et al. 2021) located on the 8.1-m Gemini-South telescope in Chile. Zorro is a fast, dual-channel speckle imager that operates at the diffraction limit for a $6.7''$ field of view. Observations were made on four individual nights: 2022-05-17, 2022-07-28, 2022-07-30, and 2023-04-08, using the 562 nm and 832 nm bands simultaneously. The techniques and procedures for observation, data reduction and image reconstruction are described in (Howell et al. 2025). Fig. 3 depicts the relative $5\text{-}\sigma$ contrast as a function of on-sky separation; no contaminants were detected within the contrast limit of $\Delta m \lesssim 5$ beyond $0.1''$.

2.6. NIRPS velocimetry

TOI-4552 was monitored simultaneously by NIRPS and HARPS from 2023 to 2024 for a total of 60 individual nights. These observations were carried out as part of the NIRPS GTO SP2 corresponding to ground-based RV follow-up of TESS planetary candidates. We used the High Efficiency instrument mode ($\lambda/\Delta\lambda \sim 75,000$) which feeds the spectrograph through a $0.9''$ fibre centred on the star and a $0.4''$ fibre observing the simultaneous sky background calibration at a separation of $39''$ on the sky from the star. The larger science fibre allows for a higher instrument throughput, important for observing faint stars such as TOI-4552. The exposure time per observation was 900 seconds and two consecutive exposures were done every night, except for one, resulting in a total of 119 individual science frames. Because the orbital period (0.3011 days) is so short, the nightly consecutive observations exhibit a slight but significant phase difference ($\sim 7\%$); we therefore choose not to bin the data.

The raw data used in our analysis was processed via the ESO supported NIRPS DRS-3.2.0 (Bouchy et al. 2025). A key challenge in near-infrared velocimetry is contamination from telluric absorption and emission lines introduced by Earth's atmosphere. Although the NIRPS DRS applies a correction for these features (Allart et al. 2022), the process is not always perfect. In particular, at times when the systemic velocity of the star (v_{sys} , see Table 1) is close to the barycentric Earth radial velocity (BERV), the stellar and telluric lines can overlap, making the correction less effective. If this overlap occurs at multiple epochs, the RV timeseries is offset and imprinted with the harmonics of the Earth's orbital period (365.24 days). This 'BERV overlap' phenomenon and ways to mitigate it are explored in detail in more recent works (Frensch et al. 2026; Parc et al. 2025; Srivastava et al. in review at A&A) as well as in Section 4.2. Alternatively, the NIRPS spectra can be extracted and processed using the APERO framework (Cook et al. 2022) which yielded results consistent with NIRPS DRS-3.2.0, therefore we choose to use the NIRPS DRS-3.2.0 data for our analysis.

The final RV extraction uses the line-by-line (LBL; `v0.65.001`) framework (Artigau et al. 2022) which has been demonstrated to work effectively in the NIR (e.g., Suárez Mascareño et al. 2025; Donati et al. 2025). Since TOI-4552 is faint, creating a high-SNR template for the RV calculation inside the LBL algorithm would be challenging; we therefore instead constructed the template from 111 NIRPS observations of GJ 643, which is much brighter ($V = 11.73$, $J = 7.55$) and similar in

spectral type (M4.5V) to TOI-4552. The LBL reported median RV uncertainty per-exposure ($\overline{\sigma_{RV}}$) for TOI-4552 is 7.7 m/s with a root-mean-square (RMS) of 9.2 m/s. A total of nine exposures of TOI-4552 acquired on 2023-04-15, 2023-04-17, 2024-07-29, 2024-08-23, 2024-09-19, 2024-10-12 and 2024-10-24 were excluded from the final analysis, corresponding to low SNR outliers ($\sigma_{RV} > 14$ m/s) attributed to poor observing conditions.

2.7. HARPS velocimetry

By design, NIRPS observations are simultaneously accompanied by HARPS, together providing a full coverage of the visible (VIS) and near-infrared (NIR) wavelength ranges. An instrumental problem with the HARPS-EGGS mode fibre shutter forced us to split the 59 total HARPS measurements between its EGGS (37 observations, $\lambda/\Delta\lambda = 80,000$) and HAM (22 observations, $\lambda/\Delta\lambda = 115,000$) instrument modes. Due to the high magnitude ($V = 14.44$) and a late stellar type (M4.5V), HARPS is unable to produce high quality radial-velocity measurements. We used the standard template matching algorithm sBART (Silva et al. 2022)³ to obtain the RVs, as it has been optimised and tested extensively on HARPS datasets. For EGGS mode observations $\overline{\sigma_{RV}}$ is 9.5 m/s with a RMS of 27.9 m/s, while the HAM mode had uncertainties three times larger. Therefore, we only use the HARPS-EGGS observations in our final analysis. The observations from the nights of 2023-04-15 and 2023-04-17 were rejected because the corresponding nights were flagged and removed from the NIRPS timeseries. The final RV timeseries for both NIRPS and HARPS is provided in Table A.1.

3. Stellar Characterization of TOI-4552

3.1. Empirically derived stellar parameters

We derived the stellar radius of TOI-4552 using its empirical relation with the K_s absolute magnitude from Mann et al. (2015) for M dwarfs, adopting the K_s magnitudes reported by 2MASS (Skrutskie et al. 2006) and the distance from Gaia DR3 parallax measurements (Gaia Collaboration et al. 2023). This yields a radius of $R_* = 0.2869 \pm 0.0088 R_\odot$. Similarly, the stellar mass was estimated using the empirical $M_* - K_s$ relation from Mann et al. (2019), giving $M_* = 0.2619 \pm 0.0063 M_\odot$. From these values, we computed the surface gravity ($\log g_* = 4.940 \pm 0.028 \text{ cm s}^{-2}$) and stellar luminosity ($L_* = 0.00836 \pm 0.0013 L_\odot$). The effective temperature ($T_{\text{eff}} = 3258 \pm 115 \text{ K}$) used in the luminosity calculation was obtained through spectroscopic analysis combined with SED fitting (see Sections 3.3, 3.2). All uncertainties were propagated using a Monte Carlo approach, and the final stellar bulk parameters are summarize in Table 1.

3.2. Spectral energy distribution fit

Stellar parameters were also derived by fitting a Spectral Energy Distribution (SED) to multi-band photometry using the Virtual Observatory Spectral Analyzer (VOSA) tool (Bayo et al. 2008). The observational data included fluxes from the GBP, G, and GRP bands from the Gaia mission (Gaia Collaboration et al. 2018), B and V from APASS (Henden et al. 2015), g' , r' and i' from SDSS Catalogue, release 12 (Alam et al. 2015), J, H and Ks from 2MASS (Skrutskie et al. 2006) and W1, W2, W3, and W4 from the WISE mission (Wright et al. 2010). VOSA performs a χ^2 minimization between the observational data and synthetic

³ <https://github.com/iaastro-pt/sBART>

Table 1: Stellar parameters for TOI-4552.

	TOI-4552	Source
Identifiers		
TIC ID	248250955	TICv8.2
2MASS ID	J17385163-4738056	2MASS
Gaia ID	5948579462188230144	Gaia DR3
Astrometric parameters		
Right ascension (J2015.5), α	17 ^h 38 ^m 51.42 ^s	Gaia DR3
Declination (J2015.5), δ	-47° 38' 13.36''	Gaia DR3
Parallax (mas)	36.556 ± 0.017	Gaia DR3
Distance (pc)	27.38±0.01	Gaia DR3
$\mu_{R.A.}$ (mas yr ⁻¹)	-134.4654 ± 0.0185	Gaia DR3
μ_{Dec} (mas yr ⁻¹)	-472.5121 ± 0.0118	Gaia DR3
v_{sys} (km s ⁻¹)	-26.2162 ± 0.9744	Gaia DR3
$U^{(\theta)}$ (km s ⁻¹)	-44.918 ± 0.923	This work
$V^{(\theta)}$ (km s ⁻¹)	-50.718 ± 0.277	This work
$W^{(\theta)}$ (km s ⁻¹)	-12.703 ± 0.146	This work
Photometric parameters		
TESS (mag)	11.9251 ± 0.0073	TICv8.2
V (mag)	14.44 ± 0.028	TICv8.2
G (mag)	13.2136 ± 0.0004	Gaia DR3
J (mag)	10.256 ± 0.021	2MASS
H (mag)	9.659 ± 0.019	2MASS
K_s (mag)	9.395 ± 0.019	2MASS
Bulk parameters		
Spectral type	M4.5V	This work
T_{eff} (K)	3258 ± 115	This work
R_* (R_\odot)	0.2869 ± 0.0088	This work
M_* (M_\odot)	0.2619 ± 0.0063	This work
ρ_* (g cm ⁻³)	15.803 ^{+1.057} _{-1.302}	This work
L_* (L_\odot)	0.00836 ± 0.0013	This work
[Fe/H] (dex)	-0.07 ± 0.09	This work
[M/H] (dex)	-0.01 ± 0.07	This work
[α /Fe] (dex)	0.06 ± 0.12	This work
Fe/Mg (mol. frac.)	0.91 ^{+0.48} _{-0.31}	This work
Mg/Si (mol. frac.)	0.62 ^{+0.69} _{-0.33}	This work
Si/O (mol. frac.)	0.10 ^{+0.1} _{-0.05}	This work
$\log g_*$ (cm s ⁻²)	4.940 ± 0.028	This work
Macroturbulence (km s ⁻¹)	4 ± 2.25	This work
Microturbulence (km s ⁻¹)	0.75 ± 0.5	This work

Sources: TICv8 (Stassun et al. 2019), 2MASS (Skrutskie et al. 2006), Gaia DR3 (Gaia Collaboration et al. 2023). ^(\theta) The values for the galactic space velocities (U, V and W) were calculated using the default function of the BANYAN Σ algorithm (Gagné et al. 2018) using parameters from Gaia DR3. The same algorithm concluded that TOI-4552 is a field star with 99.9% probability.

SEDs from theoretical models, including BT-Settl (Allard et al. 2012), Kurucz (Kurucz 1993), and Castelli & Kurucz (Castelli & Kurucz 2003). The model that provided the best fit was the BT-Settl with $T_{\text{eff}} = 3300 \pm 50 \text{ K}$, metallicity [M/H] = 0.0 dex, and surface gravity $\log(g) = 5.0 \text{ dex (cm s}^{-2}\text{)}$. The fit accounts for the observed and theoretical fluxes, their errors, the number of data points, and the object distance and radius. The resulting SED is presented in Fig. 4.

Bolometric luminosity was obtained by integrating the SED, giving $L_* = 0.00770 \pm 0.00003 L_\odot$. By using the Stefan-Boltzmann law, we obtained the stellar radius $R_* = 0.268 \pm$

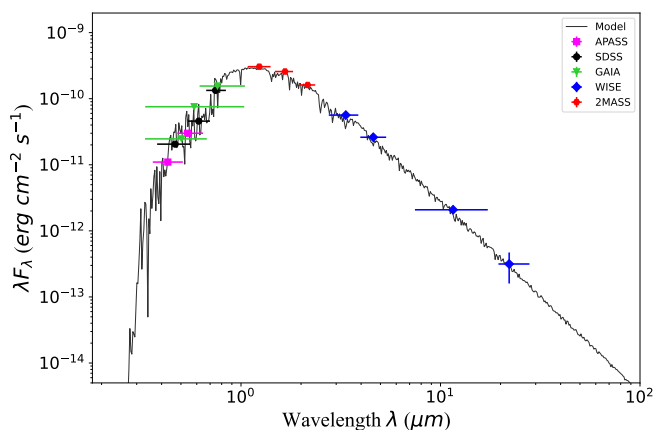


Fig. 4: Spectral Energy Distribution (SED) of TOI-4552. The best-fitting BT-Settl model (Allard et al. 2012) for parameters $T_{\text{eff}} = 3300$ K, $[M/H] = 0$ dex, and $\log g_* = 5.0$ dex is shown by the black curve. Photometric data from APASS (magenta), Gaia (green), 2MASS (red), SDSS (black), and WISE (blue) are plotted with horizontal error bars indicating the filter passbands.

Table 2: TOI-4552 stellar parameters derived by different methods.

	Empirical	SED
R_* (R_\odot)	0.2869 ± 0.0088	0.268 ± 0.008
M_* (M_\odot)	0.2619 ± 0.0063	0.259 ± 0.012
L_* (L_\odot)	0.00836 ± 0.00130	0.00770 ± 0.00003
$\log g_*$ (cm s^{-2})	4.940 ± 0.028	5.0

$0.008 R_\odot$. Finally, the stellar mass ($M_* = 0.259 \pm 0.012 M_\odot$) was estimated using Equation 6 from Schweitzer et al. (2019).

A comparison between the empirically computed stellar properties and the ones from the SED fit are showcased in Table 2. Both the mass and the radius of the star are in agreement within $1-\sigma$ between the two methods. Due to the lower uncertainties, we adopt the empirically derived stellar parameters (Table 1).

3.3. HARPS stellar analysis

To derive stellar parameters with the HARPS optical spectrum, we first combined the 33 HARPS-EGGS spectra reduced with the ESPRESSO DRS-3.2.5 pipeline (Pepe et al. 2021) repurposed to work on HARPS data (and corrected by their RV), by using the task `scombine` within IRAF⁴ to obtain a high SNR spectrum. Then, we applied the machine learning tool ODUSSEAS⁵ (Antoniadis-Karnavas et al. 2020, 2024) to derive the effective temperature (T_{eff}) and metallicity ($[\text{Fe}/\text{H}]$) from the pseudo equivalent widths (EWs) of a set of ~ 4000 lines in the optical spectra. This tool applies a machine learning model trained with the same lines measured and calibrated in a reference sample of 47 M dwarfs observed with HARPS for which their $[\text{Fe}/\text{H}]$ were obtained from photometric calibrations (Neves et al. 2012) and their T_{eff} from interferometric calibrations (Khata et al. 2021). Using this method, we derived a $T_{\text{eff}} = 3323 \pm 101$ K and $[\text{Fe}/\text{H}] = 0.00 \pm 0.12$ dex. The

⁴ IRAF is distributed by National Optical Astronomy Observatories, operated by the Association of Universities for Research in Astronomy, Inc., under contract with the National Science Foundation, USA.

⁵ <https://github.com/AlexandrosAntoniadis/ODUSSEAS>

Table 3: TOI-4552 stellar abundances measured with NIRPS.

Element	$[\text{X}/\text{H}]^*$	no. of lines
O I	-0.02 ± 0.09	31
Na I	0.23 ± 0.11	4
Mg I	-0.12 ± 0.16	1
Al I	-0.32 ± 0.08	5
Si I	0.17 ± 0.28	2
K I	-0.10 ± 0.31	8
Ca I	-0.13 ± 0.10	13
Ti I	-0.12 ± 0.12	36
Cr I	0.06 ± 0.09	14
Mn I	0.28 ± 0.12	5
Fe I	-0.07 ± 0.09	25

*Relative-to-solar abundances

same process was repeated for the same HARPS spectra reduced by the offline DRS-3.5 pipeline as well which yielded $T_{\text{eff}} = 3247 \pm 96$ K and $[\text{Fe}/\text{H}] = 0.01 \pm 0.11$.

The HARPS T_{eff} values are in agreement with the one obtained from the SED fit as well as the one reported by TESS DVR ($T_{\text{eff}} = 3265 \pm 157$ K). To accommodate the large uncertainties of each measurement, we combined the four estimates of effective temperature by performing Gaussian resampling by assuming a normal distribution for all four T_{eff} centred at the reported value and the uncertainty as the standard deviation. At each step we drew one value from each distribution, averaged them, and repeated this for 10,000 iterations. The median and $1-\sigma$ scatter of the resulting distribution give our final value of $T_{\text{eff}} = 3258 \pm 115$ K. By doing this we inflate the uncertainty in T_{eff} to account for any biases that may affect the uncertainties in the values reported by the four sources.

3.4. NIRPS stellar analysis

The stellar elemental abundances were derived from the NIRPS spectra following the methodology of Gromek et al. (in prep), based on the work of Hejazi et al. (2023), and are summarized in Table 3. We performed a spectral synthesis analysis using the order-merged telluric-corrected NIRPS template spectrum calculated within the LBL framework. Synthetic spectra were generated with MARCS stellar atmosphere models (Gustafsson et al. 2008) and the Turbospectrum radiative transfer code (Alvarez & Plez 1998; Plez 2012), implemented via modified iSpec routines (Blanco-Cuaresma 2019; Blanco-Cuaresma et al. 2014) using solar abundances from Asplund et al. (2009). The stellar parameters adopted to generate the model spectra were $T_{\text{eff}} = 3258 \pm 115$ K, $v_{\text{mac}} = 4 \pm 2.25$ km s⁻¹, and $v_{\text{mic}} = 0.75 \pm 0.5$ km s⁻¹. The macroturbulence (v_{mac}) and microturbulence (v_{mic}) velocities were determined through χ^2 -minimization of molecular OH lines, which are especially sensitive to these broadening parameters (Souto et al. 2017; Hejazi et al. 2023). Absorption lines were selected from the normalized spectrum, cross-referenced with atomic and molecular features in the VALD line-list (Kupka et al. 2011), and further refined via visual inspection to exclude blended or contaminated features. The oxygen abundance was derived from OH features.

Synthetic spectra were generated for each line by varying the elemental abundance $[\text{X}/\text{H}]$ between -0.75 and $+0.75$ dex in 0.25 dex steps which were then interpolated to 0.015 dex resolution. Best-fit abundances were obtained via χ^2 minimization between the model and observed spectrum within a fitting window. For certain lines where the continuum level between the model and

Table 4: TOI-4552 b radius derived from transit lightcurves of each individual instrument.

Instrument	δ (ppm)	R_p (R_\oplus)	no. of transits
TESS	1195 ± 89	1.083 ± 0.051	224
ExTrA	1117 ± 81	1.047 ± 0.053	61
LCO	992 ± 122	0.987 ± 0.068	6
SPECULOOS	1385 ± 129	1.161 ± 0.064	20

the spectra do not match, we fit and apply a uniform flux offset that minimizes the χ^2 between the observed data and the model in the continuum region within 0.5-nm of the spectral line. Final abundances for each element are calculated as weighted averages of the individual abundances, with the weighting equal to the RMSE between the best-fit model and the observed line in each line region, divided by the line depth. Random uncertainties (σ_{ran}) were calculated as the standard deviation of the line-by-line abundance distribution divided by \sqrt{N} , where N is the number of lines used per element. Systematic uncertainties due to T_{eff} , $[M/H]$, $\log g_*$, v_{mac} , and v_{mic} were estimated by independently resampling each stellar parameter from its Gaussian uncertainty distribution and repeating the analysis over 15 iterations (Hejazi et al. 2023). The total uncertainty is computed by summing the random and systematic components in quadrature. Global metallicity and α -enhancement was recomputed following Hinkel et al. (2022), yielding $[M/H] = -0.01 \pm 0.07$ dex from the summed number ratios of O, Na, Mg, Si, K, Ca, Ti, Cr, Mn and Fe, and $[\alpha/Fe] = 0.06 \pm 0.12$ using the alpha elements O, Mg, Si, Ca, and Ti. The final stellar abundance measurements and parameters are reported in Tables 1 and 3.

It should be noted that the best fit SED model of BT-Settl is in agreement with the spectroscopically derived T_{eff} and $[M/H]$ values for TOI-4552. We choose to report the values inferred from spectroscopic observations in Table 1.

3.5. Stellar activity

To constrain any potential stellar activity signals, we analysed the spectroscopic activity indicators in the NIRPS RV computed in the standard LBL reduction framework, namely the differential temperature metric (ΔT ; Artigau et al. 2024) and the second-order derivative of the velocity (D2V; Zechmeister et al. 2018; Artigau et al. 2022). Fig. B.2 shows the timeseries for the two indicators and the respective Lomb-Scargle periodogram. No significant peaks are detected above the 99.9% confidence level on a short time scale apart from aliases of the 1-day RV sampling. For long-term monitoring, we detected no significant trends in the TESS SAP lightcurve. However, we only have three sectors of photometric data, each separated by two years, so the sampling is insufficient to identify any definitive variability. As an alternative, we obtained the publicly available photometric measurements from the All-Sky Automated Survey for Supernovae (ASAS-SN, Kochanek et al. 2017) Sky Patrol V2.0⁶ (Hart et al. 2023; Shappee et al. 2014). These observations were done using the V and g' -band filters and are displayed in Fig. B.1 along with the periodogram. The highest detected peak is at 765-days (slightly above the 99.99% confidence level), a possible signature of magnetic activity as can be the case in late M dwarfs (Suárez Mascareño et al. 2016). However, it is of note that its period is very close to the two year harmonic of the Earth's orbital period and is thus likely an artifact of the window function.

We conclude that TOI-4552 is a quiet star with no significant short term stellar rotation period detected in RVs and TESS photometry and no obvious magnetic cycle detected in long-term photometry.

4. Transit and radial velocity analysis

4.1. Transit lightcurve analysis

TOI-4552 was observed in three TESS sectors (12, 39, and 66) and monitored from the ground with ExTrA, LCO and SPECULOOS. No additional transiting candidates or signatures of transit timing variations (TTVs) were observed in our transit sample, making TOI-4552 b the only currently detected short period transiting planet in the system. We first retrieved the TESS lightcurves using `lightkurve` (Lightkurve Collaboration et al. 2018)⁷. While these PDCSAP lightcurves were corrected for instrumental systematics, we observed additional residual correlated structures that can impact the retrieved planetary radius. We therefore used a Gaussian Process (GP) with the Matérn-3/2 kernel approximation implemented in `celerite` (Foreman-Mackey et al. 2017) available natively in `juliet` to further detrend the lightcurves. The following formalism for the term is used:

$$k(\tau) = \alpha^2 \left(1 + \frac{\sqrt{3}\tau}{\beta} \right) \exp\left(-\frac{\sqrt{3}\tau}{\beta}\right) \quad (1)$$

where α is the amplitude, β is the length scale and τ is the time lag. To prevent the GP from fitting the USP transits, we restrict the lower limit of length scale to be 1-day. The same GP kernel was used inside `Allesfitter` to detrend the SPECULOOS lightcurves (e.g., Dransfield et al. 2024; Henderson et al. 2024) as well as ExTrA lightcurves (e.g., Cointepas et al. 2021). The LCO lightcurves were detrended at the extraction phase via the `AstroImageJ` software.

Using preliminary period and time of conjunction measurements reported by SPOC ($P_{orb} = 0.3011$ days; $t_c = 2459361.8822$ BJD), we performed transit fits using `juliet` (Espinoza et al. 2019) to ensure that the retrieved radii of the planet are consistent between instruments using stellar parameters from Table 1. The two coefficient limb darkening formalism from Kipping (2013) was used and both coefficients were fit individually for each instrument. All three TESS sectors (12, 39 and 66) were modelled as independent instruments to incorporate their separate GP fits, lightcurves from LCO-CTIO and LCO-SAAO were modelled separately, all three ExTrA telescopes (ExTrA1, ExTrA2, ExTrA3) were modelled separately, and each of the SPECULOOS telescopes and the various combinations of photometric filters (Europa- g' , Europa- r' , Ganymede- r' , Io- g' , Io- r' , Io- z') were modelled as different instruments. Table 4 highlights the transit depth (δ) and planetary radius (R_p) obtained for each individual instrument as well as the number of total transits observed, which all agree within $2\text{-}\sigma$ uncertainty. It should be noted that no additional dilution correction was applied to the extracted lightcurves at this point. The same P_{orb} and t_c were later used as priors in the joint fit with RVs (see Section 4.4).

4.2. Radial velocity analysis: BERV overlap

The Earth's atmosphere is not as transparent in NIR compared to VIS wavelength range. Telluric absorption and emission features

⁶ <http://asas-sn.ifa.hawaii.edu/skypatrol/>

⁷ <https://github.com/lightkurve/lightkurve>

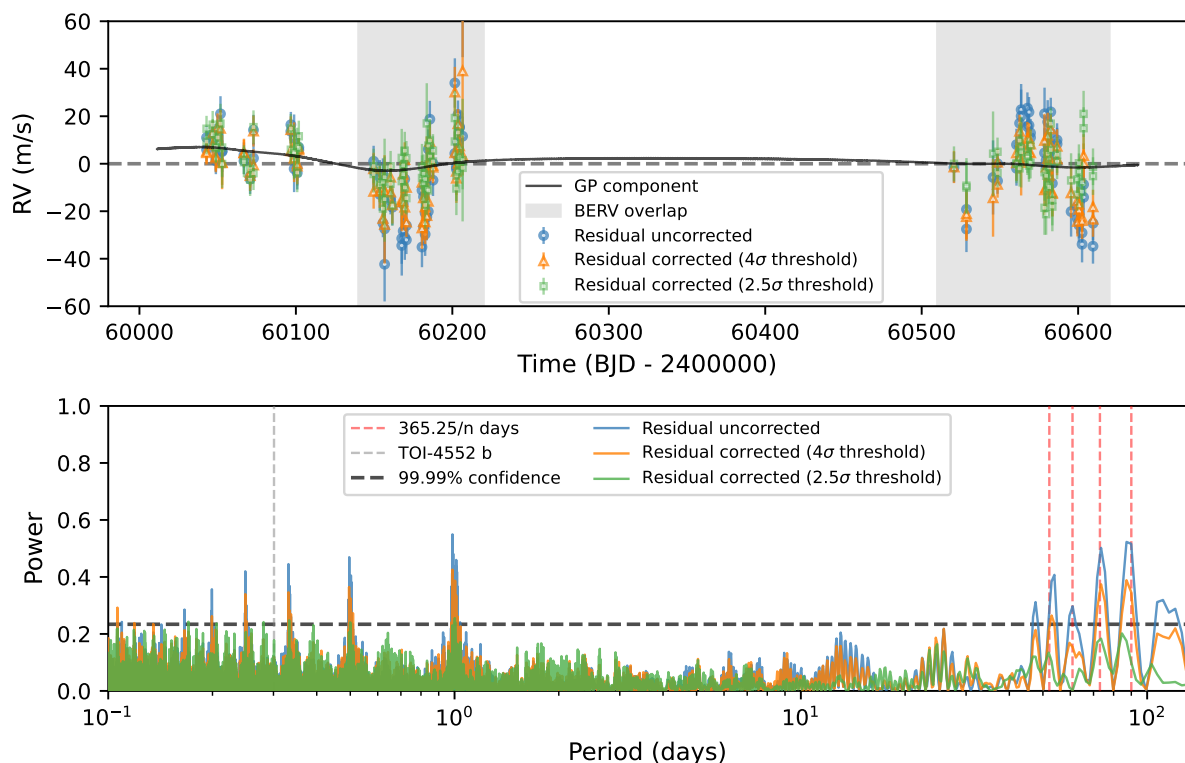


Fig. 5: NIRPS RV timeseries of TOI-4552 (top) along with the corresponding periodograms (bottom). Due to the BERV overlap issue discussed in Section 4.2, we masked a small number of pixels from each frame that contained stellar lines severely affected by under-corrected tellurics. Outlier pixels were identified using a σ -clipping threshold, such that any deviations from the median stellar spectrum exceeding the threshold were masked. We present here the unmasked (Residual uncorrected) and masked (Residual corrected) time series at 4σ and 2.5σ thresholds, along with their corresponding periodograms. After applying the 2.5σ threshold, the peaks associated with harmonics of Earth’s rotation ($365.24/n$ days) fall below the confidence level, indicating that the telluric signals have been effectively suppressed. The telluric residual corrected time series (green) is adopted for our final analysis.

pollute the entire NIR coverage of NIRPS and while we have methods of correcting them (Allart et al. 2022; Cook et al. 2022; Srivastava et al. in review), they are not perfect and may leave some residuals that are anchored in the Earth’s rest frame. The previously mentioned BERV crossing phenomenon occurs due to these anchored residuals. Following the procedure explored in Srivastava et al. (in review), we perform a post-processing reduction to mask any pixels, across all observations of TOI-4552, that exhibit variations in flux beyond a 2.5σ threshold relative to the median stellar spectrum. The value for this threshold is partly arbitrary and may not be optimal for other targets. It depends on the SNR of the science observation and the efficiency of the telluric absorption and emission corrections. This aggressive masking of pixels aims to remove telluric residuals at the expense of RV precision. An obvious signature of the dataset being contaminated by telluric residuals is the presence of harmonics of the Earth’s orbital period ($365.24/n$ days) in the periodogram. Throughout the development and testing phase of this post-processing tool we analysed the impact of differing thresholds on the RV timeseries (Fig. 5). The 2.5σ threshold was found to be optimal, as it reduced the power of the peaks associated with harmonics of Earth’s orbital period to below the 0.01% false-alarm probability (FAP; 99.99% confidence) in the periodogram.

4.3. Radial velocity analysis: Gaussian Process detrending

We also explored alternative methods to correct for the effects of telluric residuals, including the use of a Gaussian Process (GP) to detrend for the systematics. While GP hyperparameters can have a physical interpretation (Stock et al. 2023), we are using it to model systematics and therefore have to carefully choose a kernel and priors for the hyperparameters so as to not overfit the data. Here, we again used the Matern-3/2 kernel approximation available in `juliet` (see Section 4.1 for more details). The GP was applied on two datasets, one not corrected for the telluric residuals (blue points in Fig. 5) and the other corrected for those features (green points in Fig. 5). The various models and their results are displayed in Table 5.

Without correcting the BERV overlap systematics, then upon fitting the GP and planet together with wide priors, the detection of the planet is not significant and is statistically similar to the GP-only fit as per the interpretation of the $\Delta \log Z$ (Kass & Raftery 1995). Despite correcting for the BERV overlap to the best of our ability, there may remain some minor correlated noise in the RV timeseries. To account for this we tried to fit the planet with and without a GP, with the scenario of a GP + Planet fit being more statistically favoured (Table 5), stressing that the identifying the cause and correcting for the systematics is a necessary step. For this fit, the P_{orb} , t_c and instrumental white noise

Table 5: Comparing the relative Bayesian evidence ($\Delta \log Z$) between various models used to remove systematics from the radial velocity timeseries.

Model	K_p (m/s)	$\Delta \log Z$
Telluric residual uncorrected data		
GP only	–	0
Planet only	5.71 ± 1.78	-59.56 ± 0.17
GP + Planet	3.04 ± 1.31	2.81 ± 0.19
Telluric residual corrected data		
GP only	–	0
Flat line	–	-7.57 ± 0.11
Planet only	4.97 ± 1.12	0.44 ± 0.13
GP + Planet	4.24 ± 1.14	4.18 ± 0.16

jitter (σ_w) were fit as free parameters following their prior distributions used in the joint fit (see Section 4.4, Table B.1). It should be noted that for the purpose of model comparison, the results of the aforementioned table reflect the various models fit solely on the RV data. Once the best model was identified (GP + Planet on the telluric residual corrected timeseries), we used it in combination with the transit data to obtain the final parameters detailed in the next section.

4.4. Joint fit

As with the transit photometry analysis, we used *juliet* for the joint fit. Table B.1 features all the parameters, priors and posteriors used to do the analysis. The segregation of photometric instruments was identical to the one explained in Section 4.1. Since the ExTrA lightcurves were ensured to be free of any dilution and contamination effects during the extraction and detrending process, the dilution factor was fit to be unity for this dataset. For all other photometric data, we allowed the dilution factor to vary between 0.5 and 1. While TESS SPOC does correct for dilution as mentioned previously, we decided to allow a variable dilution factor to account for any imperfections. We fit a two coefficient limb darkening model implemented in *juliet* (Espinoza & Jordán 2016) using the formalism presented in Kipping (2013) for each individual telescope. The posteriors are however not very well constrained, but are consistent within uncertainties across instruments. The stellar density was calculated using the stellar mass and radius from Table 1 and we used the parametrisation suggested in Espinoza (2018) for the planetary radius and impact parameter. We additionally fixed the eccentricity to $e = 0$ and argument of periastron to $\omega = 90^\circ$ as the close proximity to the host star almost guarantees a tidally locked, non-eccentric orbit (e.g., Lyu et al. 2024). To lower the computational load, the fit was performed using detrended ExTrA, LCO and SPECULOOS lightcurves, while the TESS data was detrended simultaneously with the joint fit using the same kernel as described before (Section 4.1). As justified in Section 3.5, there are no hints of any short-term stellar activity to be fit in our data; therefore, we only use a GP to model any minor systematics as detailed in Section 4.3. An excess white noise jitter was fit for both NIRPS and HARPS separately as the instrument performances vary significantly.

To run our 1-planet model with 94 parameters, we used the built-in dynamic-dynesty sampler in *juliet* using 10,000 live points to prevent undersampling. A final planetary radius of $1.11 \pm 0.04 R_\oplus$ was obtained, corresponding to a transit depth of 1258 ± 55 ppm, consistent with measurements from indi-

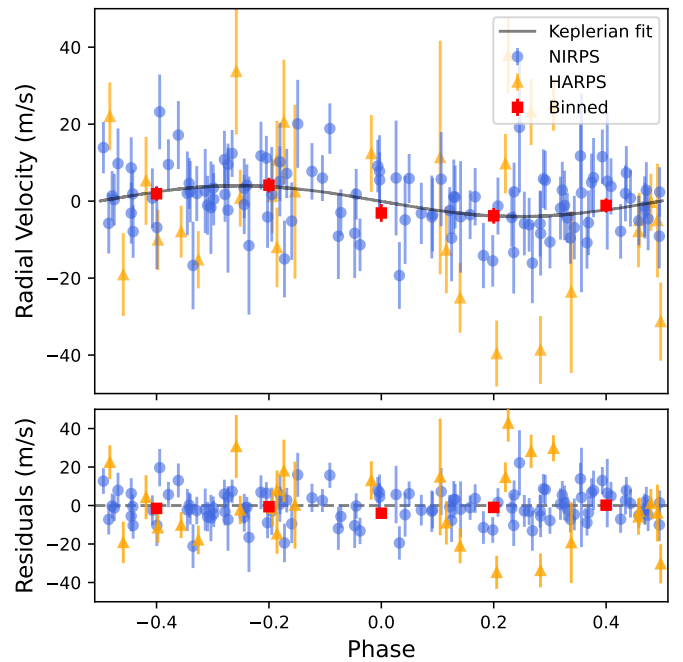


Fig. 6: *Top:* NIRPS RV measurements (blue points) and the final fit Keplerian model (grey line), phase-folded according to the P and t_c in Table 6. The red points correspond to the binned RVs. *Bottom:* Residuals of the RVs after subtracting the model.

vidual photometric instruments (see Table 4). The derived RV semi-amplitude of 4.32 ± 1.08 m/s corresponds to a mass of $1.83 \pm 0.47 M_\oplus$, a mass precision of 25% ($3.9\text{-}\sigma$). The priors and posteriors for the final fit are presented in Table B.1. It should be noted that while we use HARPS in our final analysis, the solution is primarily driven by NIRPS (see Fig. 6), thus highlighting the advantage of NIR velocimetry for M dwarf targets.

5. Discussion

5.1. TOI-4552 b composition and core mass fraction

TOI-4552 b is the eleventh rocky USP around an M dwarf star to have a constrained mass and radius measurement. The other ten (TOI-6255 b (Dai et al. 2024), GJ 367 b (Lam et al. 2021), GJ 1252 b (Shporer et al. 2020), Wolf 327 b (Murgas et al. 2024), TOI-1685 b (Hirano et al. 2021; Bluhm et al. 2021; Burt et al. 2024), LTT 3780 b (Cloutier et al. 2020), GJ 806 b (Palle et al. 2023), TOI-1634 b (Hirano et al. 2021), TOI-1075 b (Essack et al. 2023) and TOI-6324 b (Lee et al. 2025)), along with TOI-4552 b, are presented in the mass-radius diagram (Fig. 7), with the Earth-like, silicate-rich and pure iron composition lines taken from Zeng et al. (2019). The masses and radii were taken from the most up to date publication after a query search on the NASA Exoplanet Archive⁸ (Christiansen et al. 2025) for planets with an orbital period of $P < 1$ day, radius of $R < 2 R_\oplus$, a reported mass and a host star effective temperature of $T_{\text{eff}} < 4000$ K. Other USPs orbiting FGK stars are also plotted in grey to provide a comparison to the M dwarf sample.

Using the final planetary mass and radius, we derive a bulk density of 7.74 ± 2.12 g/cm³, higher but within $1\text{-}\sigma$ of that of the Earth ($\rho_\oplus = 5.51$ g/cm³). Most USPs around M dwarfs fall into

⁸ <https://exoplanetarchive.ipac.caltech.edu/>

Table 6: Planetary parameters for TOI-4552 b.

Parameter	TOI-4552 b
Orbital period, P_{orb} (days)	$0.30110032 \pm 0.00000014$
Time of conjunction, t_c (BJD)	$2459361.88587913 \pm 0.00024681$
Planet radius, R_p (R_{\oplus})	1.11 ± 0.04
Planet mass, M_p (M_{\oplus})	1.83 ± 0.47
Planet bulk density, ρ_p (g cm^{-3})	7.74 ± 2.14
RV semi-amplitude, K_p (m s^{-1})	$4.32^{+1.04}_{-1.08}$
Orbital inclination, i ($^{\circ}$)	$87.77^{+1.94}_{-1.90}$
Scaled planetary radius, R_p/R_*	$0.0352^{+0.0009}_{-0.0009}$
Impact parameter, b	$0.16^{+0.12}_{-0.11}$
Semi-major axis, a (AU)	0.0056255 ± 0.0000003
Eccentricity, e	0 (fixed)
Argument of periastron, ω (deg)	90 (fixed)
Insolation, S_p (S_{\oplus})	263 ± 40
Equilibrium temperature ^(y) , T_{eq} (K)	1122 ± 10
ESM _{7.5\mu\text{m}}} ^(y)	19.5
Dayside temperature ^(z) , T_{day} (K)	1434 ± 10
Core mass fraction, CMF	$0.55^{+0.17}_{-0.24}$

Notes: ^(y) Equilibrium temperature and Emission Spectroscopic Metric (ESM) are calculated as in [Kempton et al. \(2018\)](#), ^(z) dayside temperature is computed using Equation 8 in [Morris et al. \(2022\)](#) assuming a bond albedo of $A_B = 0$ and heat distribution factor $f = 2/3$.

either Earth-like or silicate-rich composition categories; however, GJ 367 b ($M_p = 0.63 M_{\oplus}$; $R_p = 0.69 R_{\oplus}$) stands out as distinctly iron-rich. In our own Solar System, Mercury is the prime example of a rocky planet with an overabundance of iron compared to Venus, Earth and Mars. Accordingly, planets such as GJ 367 b are often referred to as ‘‘super-Mercuries’’. Per the location in the mass-radius diagram, TOI-4552 b has a composition partway between the Earth and Mercury, similar to several other USPs around FGK stars.

To better quantify the composition of TOI-4552 b, we computed an interior structure model using the publicly available `exopie`⁹ code ([Plotnykov & Valencia 2024](#)), an updated version of the previous SUPEREARTH code ([Plotnykov & Valencia 2020](#); [Valencia et al. 2006](#)). The core mass fraction (CMF) quantifies the proportion of a planet’s total mass contained in its core, and thereby reflects the relative abundances of iron and silicates, which primarily compose the core and mantle, respectively. We first ran `exopie` assuming a completely rocky planet with no water mass fraction and a variable (0 - 20%) amount of iron in the mantle and silicon in the core. The planetary mass and radius were used as priors and no constraints were put on the composition using stellar abundance measurements (Table 3). The results can be found in the corner plot of Fig. C.1. The sampler converges on the mass and radius values that are within 1σ of our measurements. The resultant CMF of $0.54^{+0.17}_{-0.24}$ is higher than that of the Earth ($\text{CMF}_{\oplus} = 0.33$) and lower than that of Mercury ($\text{CMF}_{\text{Mercury}} = 0.7$; [Szurgot 2015](#)), however consistent with both within the uncertainties. Another relevant metric is the uncompressed density of a planet, which is a measure of the mean density at zero pressure ([Faure & Mensing 2007](#)). Again using `exopie`, we calculated the uncompressed

⁹ <https://github.com/mplotnyko/exopie>

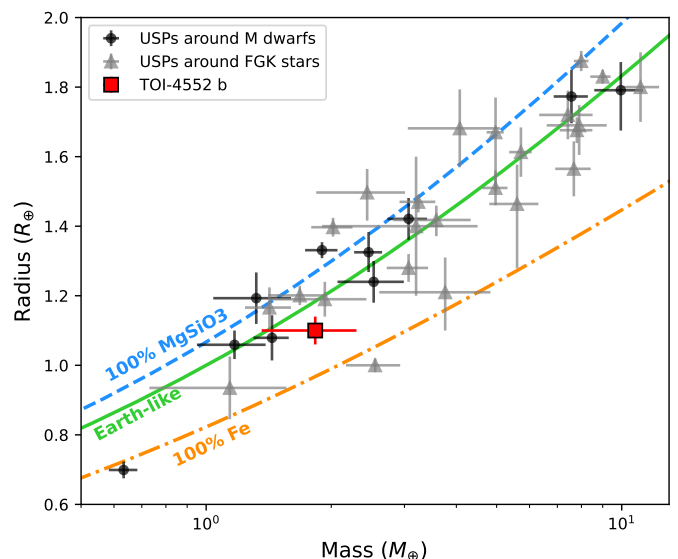


Fig. 7: Mass-Radius diagram of all rocky USPs ($R_p < 2R_{\oplus}$, $P < 1$ day) around M dwarfs ($T_{\text{eff}} < 4000$ K) and FGK stars that currently have a measured mass and radius. All planet parameters were obtained through a query search on NASA Exoplanet Archive. Silicate-rich (blue), Earth-like (green) and iron-rich (orange) compositions lines, taken from [Zeng et al. \(2019\)](#), are overplotted. According to the measured mass and radius, TOI-4552 b lies in the gap between the Earth-like and pure iron composition lines. A more precise mass measurement is required to obtain better constraints on the composition.

density of TOI-4552 b (ρ_{uncom}) to be $4.84 \pm 0.70 \text{ g/cm}^3$, lying partway between the Earth’s ($\rho_{\text{uncom,Earth}} = 4.4 \text{ g/cm}^3$) and Mercury ($\rho_{\text{uncom,Mercury}} = 5.3 \text{ g/cm}^3$; [Prentice & Jontof-Hutter 2005](#)) but consistent with both.

A common assumption when constraining planetary composition is that, since a planet and its host star form from the same interstellar medium, the planet’s refractory elemental abundances should reflect those of its star ([Dorn et al. 2015](#); [Hinkel & Unterborn 2018](#)). However, some recent works have questioned the validity of this assumption ([Santos et al. 2017](#); [Plotnykov & Valencia 2020](#); [Brinkman et al. 2024](#)) as the observations suggest that refractory ratios of rocky worlds span a larger range than that of stars. Given the slightly high CMF of TOI-4552 b, we also ran a second `exopie` model that did not use the planetary mass and radius as priors. Instead, we adopted the host star’s abundance ratios ($[\text{Fe}/\text{H}]$, $[\text{Mg}/\text{H}]$, $[\text{Si}/\text{H}]$) to predict the composition of a representative rocky planet formed around this star. Since the $[\text{Mg}/\text{H}]$ and $[\text{Si}/\text{H}]$ calculations were done using one and two spectral lines respectively, we instead use $[\alpha/\text{H}]$ as a proxy for both since they are α -elements. The result (Fig. C.2) suggests a planet with $\text{CMF} = 0.32^{+0.09}_{-0.08}$, which is just within 1σ of the CMF constrained by the mass and radius. The CMF is not constrained well enough to conclude if TOI-4552 b is an iron-rich super-Mercury or an Earth-like rocky world as both are statistically plausible from the current dataset.

The formation and evolution pathways of Mercury-like exoplanets remain uncertain. Some hypotheses, such as their being remnants of stripped gas giants ([Lin et al. 2025](#)) or products of giant impacts ([Bonomo et al. 2019](#); [Cambioni et al. 2024](#)), are considered unlikely, while other studies ([Brinkman et al. 2024](#)) find no compelling evidence for the existence of super-Mercuries at all, although GJ 367 b appears to be a strong candidate, lying close to the iron sequence of the mass-radius diagram (see

Fig. 7). Based on planet formation simulations, Mah & Bitsch (2023) propose that super-Mercuries are more likely to form around stars with low Mg/Si ratios (< 1), which is in line, albeit with large uncertainties, with the value derived from the TOI-4552 stellar spectrum analysis (Mg/Si = $0.62^{+0.67}_{-0.31}$, Table 1).

We note that Brinkman et al. (2025) reanalysed the Kepler-100 b (Weiss et al. 2024) and HD 93963A b (Serrano et al. 2022) systems using additional RV measurements from MAROON-X (Seifahrt et al. 2018) and KPF (Gibson et al. 2016). They concluded that the earlier classification of these planets as super-Mercuries was driven by low-precision mass measurements, and that with the higher-precision data the inferred CMFs are instead consistent with Earth-like values. Given the modest $3.9\text{-}\sigma$ mass detection, we cannot exclude that the mass of TOI-4552 b is slightly overestimated; several planets have had their masses revised downward as more precise RV measurements became available (e.g., LHS 1140 b Cadieux et al. 2024) and the several USPs mentioned prior (Brinkman et al. 2025). We thus conclude that despite the high density, more precise RV measurements are required to confirm or deny TOI-4552 b's status as a super-Mercury.

Could TOI-4552 b's relatively high density simply reflect an underestimated radius? A recent study (Han et al. 2025) argues that TESS radii are, on average, underestimated relative to K2/Kepler because TESS's large pixels can bias the dilution correction. This explanation seems unlikely for TOI-4552. The planetary radii inferred from the dilution-corrected TESS photometry and from ground-based observatories agree within uncertainties (see Table 4). Additionally, our final radius of $1.11 \pm 0.04 R_{\oplus}$ was calculated by allowing the dilution factor for the photometric data to be a varying parameter.

5.2. Potential tidal and rotational deformation

Since USPs are very close to their host stars, there may be non-insignificant levels of tidal deformation in these rocky planets. TOI-6255 b (Dai et al. 2024) is one such USP on the verge of tidal disruption. Based on the equations presented in Dai et al. (2024), a similar analysis can be performed for TOI-4552 b. As defined in Rappaport et al. (2013), the Roche period (P_{Roche}) is the lower limit for the orbital period before the planet is tidally disrupted. The equation:

$$P_{\text{Roche}} \approx 12.6 \text{ h} \left(\frac{\rho_{\text{P}}}{1 \text{ g/cm}^3} \right)^{-\frac{1}{2}} \quad (2)$$

approximates the Roche period (in hours), based on the planetary bulk density (ρ_{P}). For TOI-4552 b the P_{Roche} comes out to be 4.5 h. Since the orbital period (7.2 h) is higher, TOI-4552 b is likely not on the verge of tidal disruption. Furthermore, equations 4, 10 and 11 in Dai et al. (2024) can be used to estimate the fractional change in the radius of TOI-4552 b due to rotational deformation that can be probed during planetary transit. This change in radius is approximately 2.8%. With the current precision of the planetary radius being of the order of 4%, this deformational cannot be accurately measured using the current dataset.

5.3. Prospects for JWST observations

Characterizing hot rocky planets has become a defining JWST effort, reflected in focused studies (e.g., Diamond-Lowe et al. 2021; Luque et al. 2025) and the ongoing 500-hour Rocky

Worlds survey (Redfield et al. 2024). Due to their short orbital periods of less than one day, USPs are optimal targets to observe and analyse while minimizing the required telescope time. Some USPs orbiting M dwarfs have already been observed with JWST or have planned future observations: TOI-1685 b (GO3263, GO4098, GO4195; Luque et al. 2025), TOI-6255 b (GO8864), GJ 367 b (GO2508; Zhang et al. 2024), LHS 3844 b (GO1846, GO4008, GO7953) and LTT 3780 b (GO3730). TOI-4552 b joins this short list of coveted USPs for follow-up observations. Indeed, TOI-4552 b features the third shortest orbital period (comparable to those of TOI-6255 b and GJ 367 b) and a high Emission Spectroscopic Metric (ESM; Kempton et al. 2018) of 19.5 (Table 6, Fig. 8), making it a favourable USP for emission spectroscopy studies.

The leading theory of planet formation states that close-in rocky planets had their primordial H_2/He atmospheres irradiated away due to the strong X-ray/UV radiation from their M-type host stars, making a CO_2/CO dominated secondary atmosphere the likely scenario (Wordsworth & Kreidberg 2022). So far there have been no positive atmospheric detections for such worlds (Kane et al. 2020; Zhang et al. 2024; Luque et al. 2025); nevertheless, recent JWST results hint towards a possible CO_2/CO atmosphere due to vaporized surface SiO_2 around 55 Cnc e (Hu et al. 2024; Zilinskas et al. 2025).

Formation theories additionally suggest that terrestrial planets start off as molten rocks that cool down on a geological timescale. The time it takes to solidify the molten interior can range from 100 Myr (Hamano et al. 2013; Boukaré et al. 2025) to 10 Gyr (Driscoll & Barnes 2015) depending on the proximity to the host star and the orbital eccentricity of the planet. The day-side temperature of TOI-4552 b is $T_{\text{day}} = 1434 \text{ K}$, calculated using a heat redistribution factor of $f = 2/3$ following equations from López-Morales & Seager (2007); Morris et al. (2022). This temperature is too low to sustain a surface magma ocean (Elkins-Tanton 2012). However, the close-in orbit ($a = 0.0056 \text{ AU}$) and any orbital eccentricity, despite the short circularisation timescale of $t_{\text{circ}} = 0.25 \text{ Myr}$ (Heller et al. 2010; Rodríguez Martínez et al. 2023), would subject it to extreme levels of tidal forces resulting in a molten mantle, leading to a higher night-side temperature (Henning et al. 2009; Driscoll & Barnes 2015; Herath et al. 2024; Boukaré et al. 2025). This change in the night-side temperature can be probed through the shape of the phase curve and a non-zero orbital eccentricity could be measured using mid-eclipse timing. Assuming a solid mantle and no internal heating, we predict $T_{\text{night}} = 707 \text{ K}$. Any significant deviations from this value (within uncertainties) could have implications on our understanding of the evolution of such extreme rocky worlds.

In light of recent research related to the characterization of the surface material components of rocky planets with MIRI (Hu et al. 2012; Paragas et al. 2025), TOI-4552 b is a prime candidate for a phase curve study with MIRI following the recommendation by Hammond et al. (2025). Phase curves are inherently immune to the major drawbacks of transit and secondary eclipse only observations such as the Transit Light Source (TLS; Rackham et al. 2018) effect and missing the transit/eclipse due to unconstrained orbital parameters. In addition, they provide a longer, stable baseline to accurately detect any secondary eclipse or transit features. USPs constitute an attractive subclass of rocky planets which enable full phase curve measurements with a relatively modest observing time investment. Obtaining a phase curve encompassing one transit and two eclipses would constitute an optimal strategy, enabling a stable baseline for the full dataset.

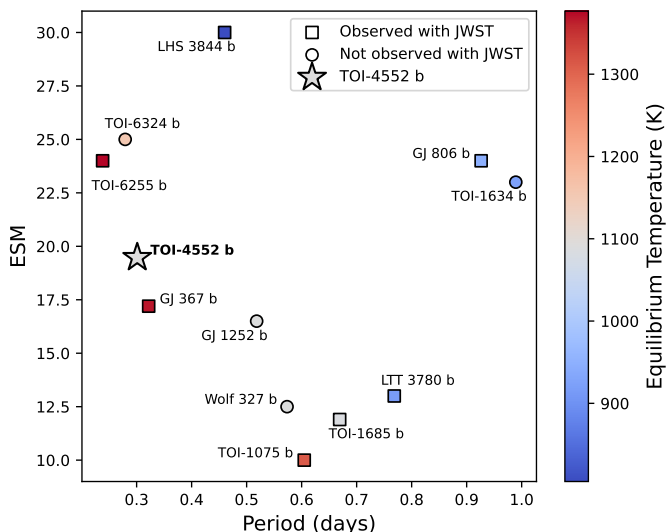


Fig. 8: Emission spectroscopic metric (ESM) versus period plot of all currently detected transiting rocky USPs with around M dwarfs with a constrained mass and radius. LHS 3844 b is additionally plotted, despite not having a published mass, as it is one of the most extensively studied USPs (Kreidberg et al. 2019). The ESMs for all planets was taken from the respective discovery publications. The colour bar indicates the equilibrium temperature and planets that have already been observed with JWST are marked as squares. TOI-4552 b has an ESM of 19.5 and the third shortest period, making it a high value target for emission spectroscopy.

6. Summary and Conclusion

We present the result of the NIRPS-GTO SP2 programme, confirmation of the planetary signal around the mid M dwarf TOI-4552. TOI-4552 b is an Earth-sized ($R_p = 1.11 \pm 0.04 R_\oplus$) planet as inferred from photometric lightcurves from TESS, ExTrA, SPECULOOS and LCO observatories. Our radial velocity analysis, which is primarily driven by NIRPS and corroborated by HARPS yields a mass of $1.83 \pm 0.47 M_\oplus$ corresponding to a bulk density of $\rho_p = 7.74 \pm 2.12 \text{ g/cm}^3$, marginally higher than the Earth’s. Both spectroscopy and short and long term photometry show no indication of stellar activity, deeming TOI-4552 as a quiet star.

Based on the planetary mass and radius we ran an interior structure model using `exopie` which favoured a CMF of $0.54^{+0.17}_{-0.25}$, partway between an Earth-like and super-Mercury composition. Additional RV measurements with greater precision (e.g., with ESPRESSO) are needed to make a definitive conclusion regarding the composition of TOI-4552 b.

With recent works focused on investigating exoplanet surface geology using JWST (e.g., Hu et al. 2012; Paragas et al. 2025), TOI-4552 b emerges as an excellent candidate. Its high emission spectroscopy metric (ESM = 19.5), likely circular orbit, ultra-short period (0.3011 days), and quiet host star make it a particularly favourable target for atmospheric and surface composition characterization with JWST.

Data availability

Table A.1 is only available in electronic form at the CDS via anonymous ftp to cdsweb.u-strasbg.fr (130.79.128.5) or <http://cdsweb.u-strasbg.fr/cgi-bin/qcat?J/A+A/>.

Acknowledgements. RD, ÉA, CC, BB, PL, AL & JPW acknowledge the financial support of the FRQ-NT through the Centre de recherche en astrophysique du Québec as well as the support from the Trotter Family Foundation and the Trotter Institute for Research on Exoplanets.

RD & ÉA acknowledges support from Canada Foundation for Innovation (CFI) program, the Université de Montréal and Université Laval, the Canada Economic Development (CED) program and the Ministère of Economy, Innovation and Energy (MEIE).

ED-M, SCB, EC & NCS acknowledge the support from FCT - Fundação para a Ciência e a Tecnologia through national funds by these grants: UIDB/04434/2020, UIDP/04434/2020.

ED-M further acknowledges the support from FCT through Stimulus FCT contract 2021.01294.CEECIND. ED-M acknowledges the support by the Ramón y Cajal contract RYC2022-035854-I funded by MICIU/AEI/10.13039/501100011033 and by ESF+.

The Board of Observational and Instrumental Astronomy (NAOS) at the Federal University of Rio Grande do Norte’s research activities are supported by continuous grants from the Brazilian funding agency CNPq. This study was partially funded by the Coordenação de Aperfeiçoamento de Pessoal de Nível Superior—Brasil (CAPES) — Finance Code 001 and the CAPES-Print program.

0

XB, XDe & TF acknowledge funding from the French ANR under contract number ANR24CE493397 (ORVET), and the French National Research Agency in the framework of the Investissements d’Avenir program (ANR-15-IDEX-02), through the funding of the “Origin of Life” project of the Grenoble-Alpes University.

SCB acknowledges the support from Fundação para a Ciência e Tecnologia (FCT) in the form of a work contract through the Scientific Employment Incentive program with reference 2023.06687.CEECIND.

NBC acknowledges support from an NSERC Discovery Grant, a Canada Research Chair, and an Arthur B. McDonald Fellowship, and thanks the Trotter Space Institute for its financial support and dynamic intellectual environment.

XDu acknowledges the support from the European Research Council (ERC) under the European Union’s Horizon 2020 research and innovation programme (grant agreement SCORE No 851555) and from the Swiss National Science Foundation under the grant SPECTRE (No 200021_215200).

This work has been carried out within the framework of the NCCR PlanetS supported by the Swiss National Science Foundation under grants 51NF40_182901 and 51NF40_205606.

DE acknowledge support from the Swiss National Science Foundation for project 200021_200726. The authors acknowledge the financial support of the SNSF.

JIGH, ASM, RR & AKS acknowledge financial support from the Spanish Ministry of Science, Innovation and Universities (MICIU) projects PID2020-117493GB-I00 and PID2023-149982NB-I00.

ICL acknowledges CNPq research fellowships (Grant No. 313103/2022-4).

BLCM acknowledge CAPES postdoctoral fellowships.

BLCM acknowledges CNPq research fellowships (Grant No. 305804/2022-7).

JRM acknowledges CNPq research fellowships (Grant No. 308928/2019-9).

CM acknowledges the funding from the Swiss National Science Foundation under grant 200021_204847 “PlanetsInTime”.

Co-funded by the European Union (ERC, FIERCE, 101052347). Views and opinions expressed are however those of the author(s) only and do not necessarily reflect those of the European Union or the European Research Council. Neither the European Union nor the granting authority can be held responsible for them.

GAW is supported by a Discovery Grant from the Natural Sciences and Engineering Research Council (NSERC) of Canada.

We acknowledge funding from the European Research Council under the ERC Grant Agreement n. 337591-ExTrA.

AL acknowledges support from the Fonds de recherche du Québec (FRQ) - Secteur Nature et technologies under file #349961.

KAM acknowledges support from the Swiss National Science Foundation (SNSF) under the Postdoc Mobility grant P500PT_230225.

AKS acknowledges financial support from La Caixa Foundation (ID 100010434) under the grant LCF/BQ/DI23/11990071.

Based on data collected by the SPECULOOS consortium. The ULiege’s contribution to SPECULOOS has received funding from the European Research Council under the European Union’s Seventh Framework Programme (FP/2007-2013) (grant Agreement n° 336480/SPECULOOS), from the Balzan Prize and Francqui Foundations, from the Belgian Scientific Research Foundation (F.R.S.-FNRS; grant n° T.0109.20), from the University of Liege, and from the ARC grant for Concerted Research Actions financed by the Wallonia-Brussels Federation. This work is supported by a grant from the Simons Foundation (PI Queloz, grant number 327127). This research is in part funded by the European Union’s Horizon 2020 research and innovation program (grants agreements n° 803193/BEBOP), and from the Science and Technology Facilities Council

(STFC; grant n° ST/S00193X/1, and ST/W000385/1)

This research has made use of the NASA Exoplanet Archive, which is operated by the California Institute of Technology, under contract with the National Aeronautics and Space Administration under the Exoplanet Exploration Program.

We acknowledge the use of public TESS data from pipelines at the TESS Science Office and at the TESS Science Processing Operations Center. Resources supporting this work were provided by the NASA High-End Computing (HEC) Program through the NASA Advanced Supercomputing (NAS) Division at Ames Research Center for the production of the SPOC data products.

References

- Alam, S., Albareti, F. D., Allende Prieto, C., et al. 2015, *ApJS*, 219, 12
- Allard, F., Homeier, D., & Freytag, B. 2012, *Philosophical Transactions of the Royal Society of London Series A*, 370, 2765
- Allart, R., Lovis, C., Faria, J., et al. 2022, *A&A*, 666, A196
- Aller, A., Lillo-Box, J., Jones, D., Miranda, L. F., & Barceló Forteza, S. 2020, *A&A*, 635, A128
- Alvarez, R., & Plez, B. 1998, *A&A*, 330, 1109
- Antoniadis-Karnavas, A., Sousa, S. G., Delgado-Mena, E., Santos, N. C., & Andersen, D. T. 2024, *A&A*, 690, A58
- Antoniadis-Karnavas, A., Sousa, S. G., Delgado-Mena, E., et al. 2020, *A&A*, 636, A9
- Artigau, É., Cadieux, C., Cook, N. J., et al. 2022, *AJ*, 164, 84
- , 2024, *AJ*, 168, 252
- Asplund, M., Grevesse, N., Sauval, A. J., & Scott, P. 2009, *ARA&A*, 47, 481
- Bayo, A., Rodrigo, C., Barrado Y Navascués, D., et al. 2008, *A&A*, 492, 277
- Blanco-Cuaresma, S. 2019, *MNRAS*, 486, 2075
- Blanco-Cuaresma, S., Soubiran, C., Heiter, U., & Jofré, P. 2014, *iSpec: Stellar atmospheric parameters and chemical abundances*, *Astrophysics Source Code Library*, record ascl:1409.006
- Bluhm, P., Pallé, E., Molaverdikhani, K., et al. 2021, *A&A*, 650, A78
- Bochanski, J. J., Hawley, S. L., Covey, K. R., et al. 2010, *AJ*, 139, 2679
- Bonfils, X., Delfosse, X., Udry, S., et al. 2013, *A&A*, 549, A109
- Bonfils, X., Almenara, J. M., Jocou, L., et al. 2015, in *Society of Photo-Optical Instrumentation Engineers (SPIE) Conference Series*, Vol. 9605, *Techniques and Instrumentation for Detection of Exoplanets VII*, ed. S. Shaklan, 96051L
- Bonomo, A. S., Zeng, L., Damasso, M., et al. 2019, *Nature Astronomy*, 3, 416
- Bouchy, F., Doyon, R., Artigau, É., et al. 2017, *The Messenger*, 169, 21
- Bouchy, F., Doyon, R., Pepe, F., et al. 2025, *A&A*, 700, A10
- Boukaré, C.-É., Lemasquiere, D., Cowan, N. B., et al. 2025, *Nature Astronomy*
- Brinkman, C. L., Polanski, A. S., Huber, D., et al. 2024, *AJ*, 168, 281
- Brinkman, C. L., Weiss, L. M., Huber, D., et al. 2025, *AJ*, 170, 109
- Brown, T. M., Baliber, N., Bianco, F. B., et al. 2013, *pas*, 125, 1031
- Burt, J. A., Hooton, M. J., Mamajek, E. E., et al. 2024, *ApJ*, 971, L12
- Cadieux, C., Plotnykov, M., Doyon, R., et al. 2024, *ApJ*, 960, L3
- Cambioni, S., Weiss, B. P., Asphaug, E., et al. 2024, in *LPI Contributions*, Vol. 3040, *55th Lunar and Planetary Science Conference*, 1360
- Castelli, F., & Kurucz, R. L. 2003, in *IAU Symposium*, Vol. 210, *Modelling of Stellar Atmospheres*, ed. N. Piskunov, W. W. Weiss, & D. F. Gray, A20
- Castro-González, A., Lillo-Box, J., Armstrong, D. J., et al. 2024, *aap*, 691, A233
- Chabrier, G. 2001, *ApJ*, 554, 1274
- Christiansen, J. L., McElroy, D. L., Harbut, M., et al. 2025, *psj*, 6, 186
- Cloutier, R., Eastman, J. D., Rodriguez, J. E., et al. 2020, *AJ*, 160, 3
- Cloutier, R., Charbonneau, D., Stassun, K. G., et al. 2021, *AJ*, 162, 79
- Cointepas, M., Almenara, J. M., Bonfils, X., et al. 2021, *A&A*, 650, A145
- Collins, K. 2019, in *American Astronomical Society Meeting Abstracts*, Vol. 233, *American Astronomical Society Meeting Abstracts #233*, 140.05
- Collins, K. A., Kielkopf, J. F., Stassun, K. G., & Hessman, F. V. 2017, *AJ*, 153, 77
- Cook, N. J., Artigau, É., Doyon, R., et al. 2022, *PASP*, 134, 114509
- Dai, F., Howard, A. W., Halverson, S., et al. 2024, *AJ*, 168, 101
- Dawson, R. I., & Fabrycky, D. C. 2010, *ApJ*, 722, 937
- Delrez, L., Gillon, M., Queloz, D., et al. 2018, in *Society of Photo-Optical Instrumentation Engineers (SPIE) Conference Series*, Vol. 10700, *Ground-based and Airborne Telescopes VII*, ed. H. K. Marshall & J. Spyromilio, 1070011
- Diamond-Lowe, H., Youngblood, A., Charbonneau, D., et al. 2021, *AJ*, 162, 10
- Donati, J. F., Cristofari, P. I., Moutou, C., et al. 2025, *A&A*, 700, A227
- Dorn, C., Khan, A., Heng, K., et al. 2015, *A&A*, 577, A83
- Dransfield, G., Timmermans, M., Triaud, A. H. M. J., et al. 2024, *MNRAS*, 527, 35
- Dressing, C. D., & Charbonneau, D. 2015, *ApJ*, 807, 45
- Driscoll, P. E., & Barnes, R. 2015, *Astrobiology*, 15, 739
- Elkins-Tanton, L. T. 2012, *Annual Review of Earth and Planetary Sciences*, 40, 113
- Espinoza, N. 2018, *Research Notes of the American Astronomical Society*, 2, 209
- Espinoza, N., & Jordán, A. 2016, *MNRAS*, 457, 3573
- Espinoza, N., Kossakowski, D., & Brahm, R. 2019, *MNRAS*, 490, 2262
- Essack, Z., Shporer, A., Burt, J. A., et al. 2023, *AJ*, 165, 47
- Faure, G., & Mensing, T. M. 2007, *Introduction to Planetary Science: The Geological Perspective*
- Foreman-Mackey, D., Agol, E., Ambikasaran, S., & Angus, R. 2017, *AJ*, 154, 220
- Frensch, Y. G. C., Bouchy, F., Lo Curto, G., et al. 2026, *A&A*, 707, A73
- Gagné, J., Mamajek, E. E., Malo, L., et al. 2018, *ApJ*, 856, 23
- Gaia Collaboration, Brown, A. G. A., Vallenari, A., et al. 2018, *A&A*, 616, A1
- Gaia Collaboration, Vallenari, A., Brown, A. G. A., et al. 2023, *A&A*, 674, A1
- Galletta, G., Colombo, S., Prisinzano, L., & Micela, G. 2025, *A&A*, 698, A180
- Gardner, J. P., Mather, J. C., Clampin, M., et al. 2006, *Space Sci. Rev.*, 123, 485
- Gardner, J. P., Mather, J. C., Abbott, R., et al. 2023, *PASP*, 135, 068001
- Gibson, S. R., Howard, A. W., Marcy, G. W., et al. 2016, in *Society of Photo-Optical Instrumentation Engineers (SPIE) Conference Series*, Vol. 9908, *Ground-based and Airborne Instrumentation for Astronomy VI*, ed. C. J. Evans, L. Simard, & H. Takami, 990870
- Gillis, E., Cloutier, R., & Pass, E. 2026, *arXiv e-prints*, arXiv:2602.23364
- Guerrero, N. M., Seager, S., Huang, C. X., et al. 2021, *ApJS*, 254, 39
- Günther, M. N., & Daylan, T. 2021, *ApJS*, 254, 13
- Gustafsson, B., Edvardsson, B., Eriksson, K., et al. 2008, *A&A*, 486, 951
- Hamano, K., Abe, Y., & Genda, H. 2013, *Nature*, 497, 607
- Hammond, M., Guimond, C. M., Lichtenberg, T., et al. 2025, *ApJ*, 978, L40
- Han, T., Robertson, P., Brandt, T. D., et al. 2025, *ApJ*, 988, L4
- Hart, K., Shappee, B. J., Hey, D., et al. 2023, *arXiv e-prints*, arXiv:2304.03791
- Hejazi, N., Crossfield, I. J. M., Nordlander, T., et al. 2023, *ApJ*, 949, 79
- Heller, R., Jackson, B., Barnes, R., Greenberg, R., & Homeier, D. 2010, *A&A*, 514, A22
- Henden, A. A., Levine, S., Terrell, D., & Welch, D. L. 2015, in *American Astronomical Society Meeting Abstracts*, Vol. 225, *American Astronomical Society Meeting Abstracts #225*, 336.16
- Henderson, B. A., Casewell, S. L., Goad, M. R., et al. 2024, *MNRAS*, 530, 318
- Henning, W. G., O'Connell, R. J., & Sasselov, D. D. 2009, *ApJ*, 707, 1000
- Herath, M., Boukaré, C.-É., & Cowan, N. B. 2024, *arXiv e-prints*, arXiv:2409.11459
- Hinkel, N. R., & Unterborn, C. T. 2018, *ApJ*, 853, 83
- Hinkel, N. R., Young, P. A., & Wheeler, III, C. H. 2022, *AJ*, 164, 256
- Hirano, T., Livingston, J. H., Fukui, A., et al. 2021, *AJ*, 162, 161
- Howell, S. B., Martínez-Vázquez, C. E., Furlan, E., et al. 2025, *Frontiers in Astronomy and Space Sciences*, 12, 1608411
- Hu, R., Ehlmann, B. L., & Seager, S. 2012, *ApJ*, 752, 7
- Hu, R., Bello-Arufe, A., Zhang, M., et al. 2024, *Nature*, 630, 609
- Jenkins, J. M., Twicken, J. D., McCauliff, S., et al. 2016, in *Society of Photo-Optical Instrumentation Engineers (SPIE) Conference Series*, Vol. 9913, *Software and Cyberinfrastructure for Astronomy IV*, ed. G. Chiozzi & J. C. Guzman, 99133E
- Kane, S. R., Roettenbacher, R. M., Unterborn, C. T., Foley, B. J., & Hill, M. L. 2020, *psj*, 1, 36
- Kass, R. E., & Raftery, A. E. 1995, *Journal of the American Statistical Association*, 90, 773
- Kempton, E. M. R., Bean, J. L., Louie, D. R., et al. 2018, *pas*, 130, 114401
- Khata, D., Mondal, S., Das, R., & Baug, T. 2021, *MNRAS*, 507, 1869
- Kipping, D. M. 2013, *MNRAS*, 435, 2152
- Kochanek, C. S., Shappee, B. J., Stanek, K. Z., et al. 2017, *pas*, 129, 104502
- Kreidberg, L., Koll, D. D. B., Morley, C., et al. 2019, *Nature*, 573, 87
- Kupka, F., Dubernet, M. L., & VAMDC Collaboration. 2011, *Baltic Astronomy*, 20, 503
- Kurucz, R. L. 1993, *SYNTHES spectrum synthesis programs and line data*
- Lam, K. W. F., Csizmadia, S., Astudillo-Defru, N., et al. 2021, *Science*, 374, 1271
- Lee, R. A., Dai, F., Howard, A. W., et al. 2025, *ApJ*, 983, L36
- Lightcurve Collaboration, Cardoso, J. V. d. M., Hedges, C., et al. 2018, *Lightkurve: Kepler and TESS time series analysis in Python*, *Astrophysics Source Code Library*
- Lin, Z., Cambioni, S., & Seager, S. 2025, *ApJ*, 978, L41
- López-Morales, M., & Seager, S. 2007, *ApJ*, 667, L191
- Luque, R., Coy, B. P., Xue, Q., et al. 2025, *AJ*, 170, 49
- Lyu, X., Koll, D. D. B., Cowan, N. B., et al. 2024, *ApJ*, 964, 152
- Mah, J., & Bitsch, B. 2023, *A&A*, 673, A17
- Mann, A. W., Feiden, G. A., Gaidos, E., Boyajian, T., & von Braun, K. 2015, *ApJ*, 804, 64
- Mann, A. W., Dupuy, T., Kraus, A. L., et al. 2019, *ApJ*, 871, 63
- Mayor, M., Pepe, F., Queloz, D., et al. 2003, *The Messenger*, 114, 20
- McArthur, B. E., Endl, M., Cochran, W. D., et al. 2004, *ApJ*, 614, L81

- McCully, C., Volgenau, N. H., Harbeck, D.-R., et al. 2018, in Society of Photo-Optical Instrumentation Engineers (SPIE) Conference Series, Vol. 10707, Software and Cyberinfrastructure for Astronomy V, ed. J. C. Guzman & J. Ibsen, 107070K
- Mignon, L., Meunier, N., Delfosse, X., et al. 2023, *A&A*, 675, A168
- Morris, B. M., Heng, K., Jones, K., et al. 2022, *A&A*, 660, A123
- Morris, R. L., Twicken, J. D., Smith, J. C., et al. 2020, *Kepler Data Processing Handbook: Photometric Analysis*, Kepler Science Document KSCI-19081-003, id. 6. Edited by Jon M. Jenkins.
- Murgas, F., Pallé, E., Orell-Miquel, J., et al. 2024, *A&A*, 684, A83
- Neves, V., Bonfils, X., Santos, N. C., et al. 2012, *A&A*, 538, A25
- Palle, E., Orell-Miquel, J., Brady, M., et al. 2023, *A&A*, 678, A80
- Paragas, K., Knutson, H. A., Hu, R., et al. 2025, *ApJ*, 981, 130
- Parc, L., Bouchy, F., Cook, N. J., et al. 2025, *A&A*, 702, A138
- Pepe, F., Cristiani, S., Rebolo, R., et al. 2021, *A&A*, 645, A96
- Plez, B. 2012, *Turbospectrum: Code for spectral synthesis*, Astrophysics Source Code Library, record ascl:1205.004
- Plotnikov, M., & Valencia, D. 2020, *MNRAS*, 499, 932
- . 2024, *MNRAS*, 530, 3488
- Prentice, A. J. R., & Jontof-Hutter, D. 2005, *Highlights of Astronomy*, 13, 73
- Rackham, B. V., Apai, D., & Giampapa, M. S. 2018, *ApJ*, 853, 122
- Rajpurohit, A. S., Kumar, V., Srivastava, M. K., et al. 2025, *A&A*, 704, A154
- Rappaport, S., Sanchis-Ojeda, R., Rogers, L. A., Levine, A., & Winn, J. N. 2013, *ApJ*, 773, L15
- Redfield, S., Batalha, N., Benneke, B., et al. 2024, arXiv e-prints, arXiv:2404.02932
- Ricker, G. R., Winn, J. N., Vanderspek, R., et al. 2015, *Journal of Astronomical Telescopes, Instruments, and Systems*, 1, 014003
- Rodríguez Martínez, R., Gaudi, B. S., Schulze, J. G., et al. 2023, *AJ*, 165, 97
- Roettenbacher, R. M., & Kane, S. R. 2017, *ApJ*, 851, 77
- Santos, N. C., Adibekyan, V., Dorn, C., et al. 2017, *A&A*, 608, A94
- Schweitzer, A., Passegger, V. M., Cifuentes, C., et al. 2019, *A&A*, 625, A68
- Scott, N. J., Howell, S. B., Gillika, C. L., et al. 2021, *Frontiers in Astronomy and Space Sciences*, 8, 138
- Seifahrt, A., Stürmer, J., Bean, J. L., & Schwab, C. 2018, in Society of Photo-Optical Instrumentation Engineers (SPIE) Conference Series, Vol. 10702, Ground-based and Airborne Instrumentation for Astronomy VII, ed. C. J. Evans, L. Simard, & H. Takami, 107026D
- Serrano, L. M., Gandolfi, D., Hoyer, S., et al. 2022, *A&A*, 667, A1
- Shappee, B. J., Prieto, J. L., Grupe, D., et al. 2014, *ApJ*, 788, 48
- Shporer, A., Collins, K. A., Astudillo-Defru, N., et al. 2020, *ApJ*, 890, L7
- Silva, A. M., Faria, J. P., Santos, N. C., et al. 2022, *A&A*, 663, A143
- Skrutskie, M. F., Cutri, R. M., Stiening, R., et al. 2006, *AJ*, 131, 1163
- Smith, J. C., Stumpe, M. C., Van Cleve, J. E., et al. 2012, *pasf*, 124, 1000
- Souto, D., Cunha, K., García-Hernández, D. A., et al. 2017, *ApJ*, 835, 239
- Stassun, K. G., Oelkers, R. J., Paegert, M., et al. 2019, *AJ*, 158, 138
- Stock, S., Kemmer, J., Kossakowski, D., et al. 2023, *A&A*, 674, A108
- Stumpe, M. C., Smith, J. C., Catanzarite, J. H., et al. 2014, *pasf*, 126, 100
- Stumpe, M. C., Smith, J. C., Van Cleve, J. E., et al. 2012, *pasf*, 124, 985
- Suárez Mascareño, A., Rebolo, R., & González Hernández, J. I. 2016, *A&A*, 595, A12
- Suárez Mascareño, A., Artigau, É., Mignon, L., et al. 2025, *A&A*, 700, A11
- Szurgot, M. 2015, in *LPI Contributions*, Vol. 1839, Comparative Tectonic and Geodynamics of Venus, Earth and Rocky Exoplanets, ed. LPI Editorial Board, 5001
- Twicken, J. D., Clarke, B. D., Bryson, S. T., et al. 2010, in Society of Photo-Optical Instrumentation Engineers (SPIE) Conference Series, Vol. 7740, Software and Cyberinfrastructure for Astronomy, ed. N. M. Radziwill & A. Bridger, 774023
- Twicken, J. D., Catanzarite, J. H., Clarke, B. D., et al. 2018, *pasf*, 130, 064502
- Valencia, D., O'Connell, R. J., & Sasselov, D. 2006, *Icarus*, 181, 545
- Weiss, L. M., Isaacson, H., Howard, A. W., et al. 2024, *ApJS*, 270, 8
- Wordsworth, R., & Kreidberg, L. 2022, *ARA&A*, 60, 159
- Wright, E. L., Eisenhardt, P. R. M., Mainzer, A. K., et al. 2010, *AJ*, 140, 1868
- Zechmeister, M., Reiners, A., Amado, P. J., et al. 2018, *A&A*, 609, A12
- Zeng, L., Jacobsen, S. B., Sasselov, D. D., et al. 2019, *Proceedings of the National Academy of Science*, 116, 9723
- Zhang, M., Hu, R., Inglis, J., et al. 2024, *ApJL*, 961, L44
- Zilinskas, M., van Buchem, C. P. A., Zieba, S., et al. 2025, *A&A*, 697, A34
- ⁵Centro de Astrobiología (CAB), CSIC-INTA, Camino Bajo del Castillo s/n, 28692, Villanueva de la Cañada (Madrid), Spain
- ⁶Instituto de Astrofísica e Ciências do Espaço, Universidade do Porto, CAUP, Rua das Estrelas, 4150-762 Porto, Portugal
- ⁷Departamento de Física Teórica e Experimental, Universidade Federal do Rio Grande do Norte, Campus Universitário, Natal, RN, 59072-970, Brazil
- ⁸Univ. Grenoble Alpes, CNRS, IPAG, F-38000 Grenoble, France
- ⁹Departamento de Física e Astronomia, Faculdade de Ciências, Universidade do Porto, Rua do Campo Alegre, 4169-007 Porto, Portugal
- ¹⁰Department of Earth, Planetary, and Space Sciences, University of California, Los Angeles, CA 90095, USA
- ¹¹Department of Physics, University of Toronto, Toronto, ON M5S 3H4, Canada
- ¹²Department of Physics, McGill University, 3600 rue University, Montréal, QC, H3A 2T8, Canada
- ¹³Department of Earth & Planetary Sciences, McGill University, 3450 rue University, Montréal, QC, H3A 0E8, Canada
- ¹⁴Centre Vie dans l'Univers, Faculté des sciences de l'Université de Genève, Quai Ernest-Ansermet 30, 1205 Geneva, Switzerland
- ¹⁵Instituto de Astrofísica de Canarias (IAC), Calle Vía Láctea s/n, 38205 La Laguna, Tenerife, Spain
- ¹⁶Departamento de Astrofísica, Universidad de La Laguna (ULL), 38206 La Laguna, Tenerife, Spain
- ¹⁷Space Research and Planetary Sciences, Physics Institute, University of Bern, Gesellschaftsstrasse 6, 3012 Bern, Switzerland
- ¹⁸Consejo Superior de Investigaciones Científicas (CSIC), E-28006 Madrid, Spain
- ¹⁹Bishop's University, Dept of Physics and Astronomy, Johnson-104E, 2600 College Street, Sherbrooke, QC, Canada, J1M 1Z7, Canada
- ²⁰Department of Physics, Engineering Physics, and Astronomy, Queen's University, 99 University Avenue, Kingston, ON K7L 3N6, Canada
- ²¹Department of Physics and Space Science, Royal Military College of Canada, 13 General Crerar Cres., Kingston, ON K7P 2M3, Canada
- ²²Center for astrophysics | Harvard & Smithsonian, 60 Garden Street, Cambridge, MA 02138, USA
- ²³American Association of Variable Star Observers, Cambridge, USA
- ²⁴Department of Physics, University of Oxford, Oxford OX13RH, UK
- ²⁵LESIA, Observatoire de Paris, CNRS, Université Paris Diderot, Université Pierre et Marie Curie, 5 place Jules Janssen, 92190 Meudon, France
- ²⁶AIM, CEA, CNRS, Université Paris-Saclay, Université de Paris, F-91191 Gif-sur-Yvette, France
- ²⁷Department of Physics and Astronomy, The University of New Mexico, 210 Yale Blvd NE, Albuquerque, NM 87106, USA
- ²⁸SETI Institute, Mountain View, CA 94043, USA NASA Ames Research Center, Moffett Field, CA 94035, USA
- ²⁹Department of Physics, The University of Warwick, Gibbet Hill Road, Coventry, CV4 7AL, UK
- ³⁰Space Telescope Science Institute, 3700 San Martin Drive, Baltimore, MD, 21218, USA
- ³¹School of Physics & Astronomy, University of Birmingham, Edgbaston, Birmingham B15 2TT, United Kingdom
- ³²Department of Physics and Kavli Institute for Astrophysics and Space Research, Massachusetts Institute of Technology, Cambridge, MA 02139, USA
- ³³Astrobiology Research Unit, Université de Liège, 19C Allée du 6 Août, 4000 Liège, Belgium
- *e-mail: avidaan.srivastava@umontreal.ca

¹Institut Trottier de recherche sur les exoplanètes, Département de Physique, Université de Montréal, Montréal, Québec, Canada

²Observatoire du Mont-Mégantic, Québec, Canada

³Observatoire de Genève, Département d'Astronomie, Université de Genève, Chemin Pegasi 51, 1290 Versoix, Switzerland

⁴Department of Physics & Astronomy, McMaster University, 1280 Main St W, Hamilton, ON, L8S 4L8, Canada

Appendix A: Supplementary data

The TESS target pixel files with the major contamination sources are depicted in Fig. A.1. Ground based photometric phasefolded lightcurves are shown in Fig. A.2. Table A.1 provides the HARPS and NIRPS timeseries corrected for tellurics used in this analysis.

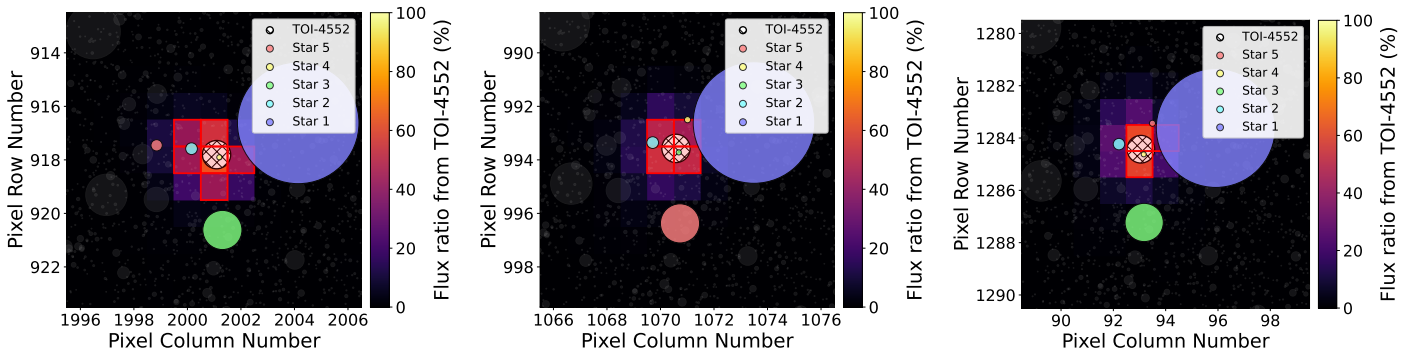


Fig. A.1: TESS target pixel file (TPF) of TOI-4552 from sectors 12 (left), 39 (centre) and 66 (right), created with TESS-cont (Castro-González et al. 2024). The aperture mask is highlighted in red and the pixel size is 21". TOI-4552 is highlighted in white with the mesh pattern. The heatmap depicts the per-pixel relative flux contributed by TOI-4552, used to optimise the aperture mask. The five stars that contaminate the lightcurve of TOI-4552 the most are highlighted, with the size of the source being a relative measure of the contamination. The TESS SPOC lightcurves are already corrected for the dilution effect from these five sources.

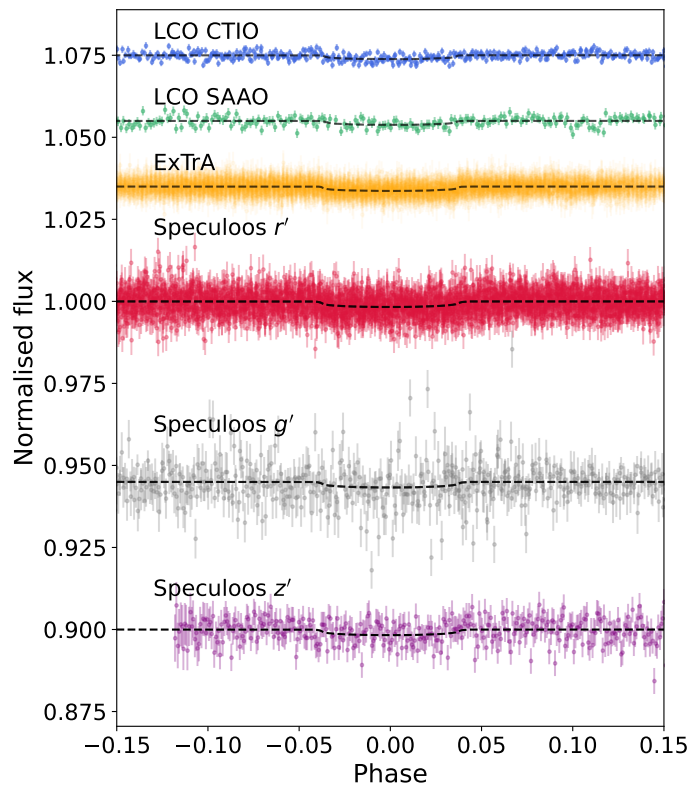


Fig. A.2: Ground based photometry of TOI-4552 separated by instruments and photometric bands. All lightcurves are phasefolded to reflect the transit feature. Any offsets in the normalised flux axis are purely to represent all datasets within the same plot and are not representative of instrument-relative flux.

Table A.1: Radial velocity timeseries of NIRPS and HARPS used for the analysis (corrected for BERV crossing systematics).

Time (BJD)	ΔRV (m/s)	σ_{RV} (m/s)	ΔT_{3000K} (K)	$\sigma_{\Delta T}$ (K)	D2V (m^2/s^2)	σ_{D2V} (m^2/s^2)	Instrument
2460042.8854	7.90	5.42	25.43	1.0	292288.88	8872.02	NIRPS
...

Notes: ΔRV is the median subtracted relative radial velocity. The median systemic velocity for NIRPS is -25490.83 m/s and for HARPS is -25247.14 m/s.

Appendix B: Stellar activity and joint fit table

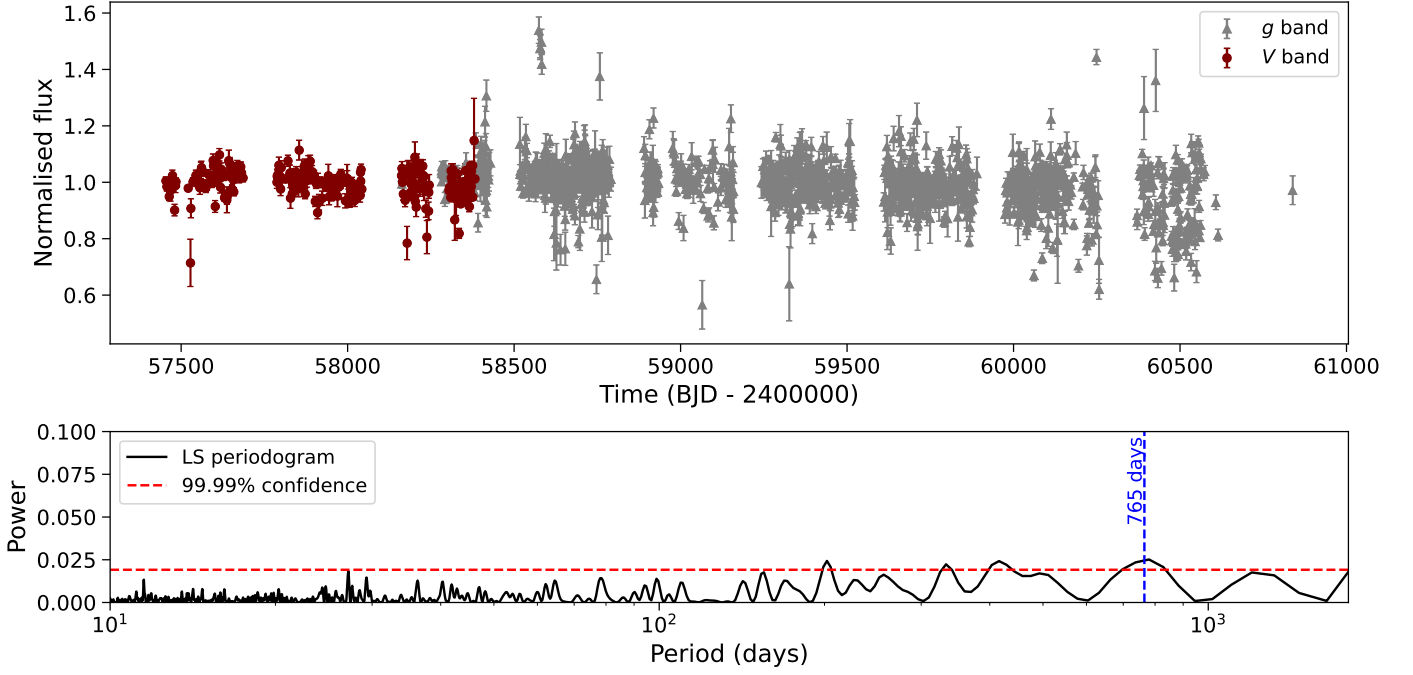


Fig. B.1: Long-term photometric monitoring of TOI-4552 done as part of the ASAS-SN survey (Kochanek et al. 2017). The data was recorded in the V and g' photometric bands. The periodogram peaks at a signal of 765 days, very close to the two year harmonic of Earth's orbital period, and likely an artifact of the window function. No other significant peaks are present that can be attributed to stellar rotation or magnetic cycle, thus TOI-4552 is a quiet star.

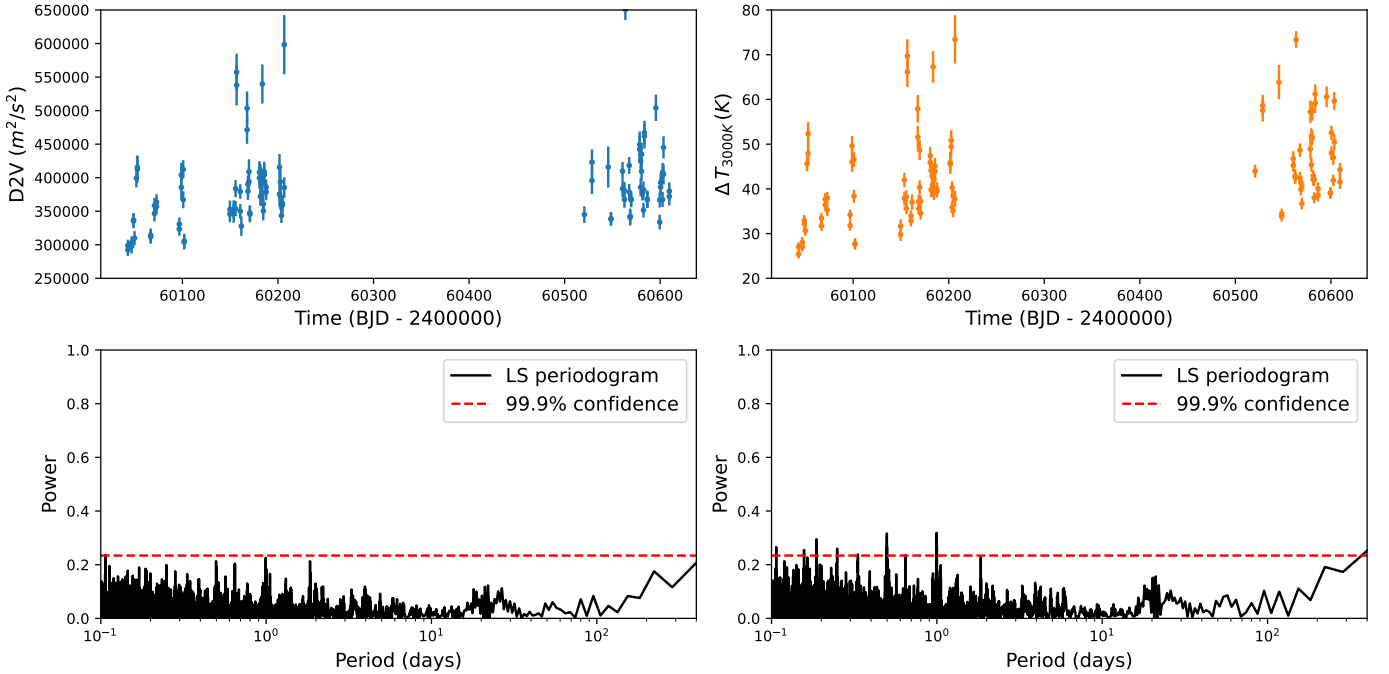


Fig. B.2: *Left:* Second-order derivative of the velocity (top) and its respective periodogram (bottom). *Right:* Differential temperature metric (top) and its periodogram (bottom). Both quantities are stellar activity indicators reported as part of the standard LBL RV extraction process (Artigau et al. 2022, 2024) for NIRPS and show no clear peaks in the periodogram that might correspond to any activity signal.

Table B.1: Median values and 68% confidence intervals of the posterior distributions of the joint fit.

Parameter	Prior	Posterior
Common transit parameters		
r_1	$\mathcal{U}(0, 1)$	$0.438^{+0.051}_{-0.052}$
Scaled planetary radius, $R_p/R_* = r_2$	$\mathcal{U}(0, 1)$	$0.0355^{+0.0008}_{-0.0008}$
Eccentricity, e	Fixed	0.0
Argument of periastron, ω (deg)	Fixed	90.0
Stellar density, ρ_* (g/cm^3)	$\mathcal{N}(15.630, 1.513)$	$16.059^{+0.700}_{-0.661}$
Orbital period, P (days)	$\mathcal{N}(0.3011, 0.001)$	$0.30110023 \pm 0.00000012$
Transit epoch, t_c (BJD)	$\mathcal{N}(2459361.8822, 0.1)$	$2459361.88588 \pm 0.00022$
TESS transit parameters		
$q_{1,\text{TESS-S12}}$	$\mathcal{U}(0, 1)$	$0.536^{+0.222}_{-0.219}$
$q_{2,\text{TESS-S12}}$	$\mathcal{U}(0, 1)$	$0.625^{+0.231}_{-0.258}$
Dilution factor, $D_{\text{TESS-S12}}$	$\mathcal{U}(0.5, 1)$	$0.861^{+0.076}_{-0.077}$
Offset relative flux, $M_{\text{TESS-S12}}$	$\mathcal{N}(0, 0.1)$	-0.0012 ± 0.0003
Jitter, $\sigma_{w,\text{TESS-S12}}$ (ppm)	$\mathcal{L}(10^{-5}, 1000)$	$3.323^{+55.673}_{-3.257}$
GP amplitude, $\alpha_{\text{TESS-S12}}$ (m/s)	$\mathcal{L}(10^{-5}, 1)$	$0.0081^{+0.0069}_{-0.0018}$
GP length scale, $\beta_{\text{TESS-S12}}$ (days)	$\mathcal{U}(1, 30)$	$1.205^{+0.795}_{-0.163}$
$q_{1,\text{TESS-S39}}$	$\mathcal{U}(0, 1)$	$0.569^{+0.207}_{-0.207}$
$q_{2,\text{TESS-S39}}$	$\mathcal{U}(0, 1)$	$0.608^{+0.239}_{-0.275}$
Dilution factor, $D_{\text{TESS-S39}}$	$\mathcal{U}(0.5, 1)$	$0.867^{+0.069}_{-0.075}$
Offset relative flux, $M_{\text{TESS-S39}}$	$\mathcal{N}(0, 0.1)$	-0.00031 ± 0.0025
Jitter, $\sigma_{w,\text{TESS-S39}}$ (ppm)	$\mathcal{L}(10^{-5}, 1000)$	$0.638^{+25.210}_{-0.633}$
GP amplitude, $\alpha_{\text{TESS-S39}}$ (m/s)	$\mathcal{L}(10^{-5}, 1)$	$0.0015^{+0.0031}_{-0.0009}$
GP length scale, $\beta_{\text{TESS-S39}}$ (days)	$\mathcal{U}(1, 30)$	$5.359^{+7.691}_{-3.875}$
$q_{1,\text{TESS-S66}}$	$\mathcal{U}(0, 1)$	$0.496^{+0.251}_{-0.249}$
$q_{2,\text{TESS-S66}}$	$\mathcal{U}(0, 1)$	$0.398^{+0.269}_{-0.228}$
Dilution factor, $D_{\text{TESS-S66}}$	$\mathcal{U}(0.5, 1)$	$0.839^{+0.079}_{-0.078}$
Offset relative flux, $M_{\text{TESS-66}}$	$\mathcal{N}(0, 0.1)$	-0.0015 ± 0.0014
Jitter, $\sigma_{w,\text{TESS-S66}}$ (ppm)	$\mathcal{L}(0.1, 100000)$	$0.157^{+212.789}_{-0.156}$
GP amplitude, $\alpha_{\text{TESS-S66}}$ (m/s)	$\mathcal{L}(10^{-5}, 1)$	$0.0043^{+0.0007}_{-0.0005}$
GP length scale, $\beta_{\text{TESS-S66}}$ (days)	$\mathcal{U}(1, 30)$	$1.089^{+0.115}_{-0.065}$
ExTrA transit parameters		
$q_{1,\text{ExTrA-T1}}$	$\mathcal{U}(0, 1)$	$0.299^{+0.272}_{-0.190}$
$q_{2,\text{ExTrA-T1}}$	$\mathcal{U}(0, 1)$	$0.496^{+0.270}_{-0.281}$
Dilution factor, $D_{\text{ExTrA-T1}}$	Fixed	1.0
Offset relative flux, $M_{\text{ExTrA-T1}}$	$\mathcal{N}(0, 0.1)$	-0.00001 ± 0.00006
Jitter, $\sigma_{w,\text{ExTrA-T1}}$ (ppm)	$\mathcal{L}(10^{-5}, 1000)$	$0.618^{+17.711}_{-0.609}$
$q_{1,\text{ExTrA-T2}}$	$\mathcal{U}(0, 1)$	$0.457^{+0.286}_{-0.293}$
$q_{2,\text{ExTrA-T2}}$	$\mathcal{U}(0, 1)$	$0.250^{+0.293}_{-0.179}$
Dilution factor, $D_{\text{ExTrA-T2}}$	Fixed	1.0
Offset relative flux, $M_{\text{ExTrA-T2}}$	$\mathcal{N}(0, 0.1)$	0.00000 ± 0.00004
Jitter, $\sigma_{w,\text{ExTrA-T2}}$ (ppm)	$\mathcal{L}(10^{-5}, 1000)$	$0.051^{+2.992}_{-0.050}$
$q_{1,\text{ExTrA-T3}}$	$\mathcal{U}(0, 1)$	$0.421^{+0.308}_{-0.268}$
$q_{2,\text{ExTrA-T3}}$	$\mathcal{U}(0, 1)$	$0.300^{+0.252}_{-0.195}$
Dilution factor, $D_{\text{ExTrA-T3}}$	Fixed	1.0
Offset relative flux, $M_{\text{ExTrA-T3}}$	$\mathcal{N}(0, 0.1)$	-0.00005 ± 0.00003
Jitter, $\sigma_{w,\text{ExTrA-T3}}$ (ppm)	$\mathcal{L}(10^{-5}, 1000)$	$0.001^{+0.045}_{-0.001}$
LCO transit parameters		
$q_{1,\text{LCO-CTIO}}$	$\mathcal{U}(0, 1)$	$0.526^{+0.251}_{-0.255}$
$q_{2,\text{LCO-CTIO}}$	$\mathcal{U}(0, 1)$	$0.411^{+0.259}_{-0.241}$
Dilution factor, $D_{\text{LCO-CTIO}}$	$\mathcal{U}(0.5, 1)$	$0.749^{+0.078}_{-0.076}$

Table B.1: continued.

Parameter	Prior	Posterior
Offset relative flux, $M_{\text{LCO-CTIO}}$	$\mathcal{N}(0, 0.1)$	0.00001 ± 0.00005
Jitter, $\sigma_{w,\text{LCO-CTIO}}$ (ppm)	$\mathcal{L}(10^{-5}, 1000)$	$0.116^{+14.791}_{-0.115}$
$q_{1,\text{LCO-SAAO}}$	$\mathcal{U}(0, 1)$	$0.489^{+0.248}_{-0.242}$
$q_{2,\text{LCO-SAAO}}$	$\mathcal{U}(0, 1)$	$0.555^{+0.229}_{-0.248}$
Dilution factor, $D_{\text{LCO-SAAO}}$	$\mathcal{U}(0.5, 1)$	$0.775^{+0.117}_{-0.118}$
Offset relative flux, $M_{\text{LCO-SAAO}}$	$\mathcal{N}(0, 0.1)$	0.00003 ± 0.00010
Jitter, $\sigma_{w,\text{LCO-SAAO}}$ (ppm)	$\mathcal{L}(10^{-5}, 1000)$	$0.137^{+15.483}_{-0.136}$
SPECULOOS transit parameters		
$q_{1,\text{SPECULOOS-}E_{g'}}$	$\mathcal{U}(0, 1)$	$0.626^{+0.223}_{-0.265}$
$q_{2,\text{SPECULOOS-}E_{g'}}$	$\mathcal{U}(0, 1)$	$0.561^{+0.266}_{-0.298}$
Dilution factor, $D_{\text{SPECULOOS-}E_{g'}}$	$\mathcal{U}(0.5, 1)$	$0.702^{+0.112}_{-0.110}$
Offset relative flux, $M_{\text{SPECULOOS-}E_{g'}}$	$\mathcal{N}(0, 0.1)$	0.00017 ± 0.00025
Jitter, $\sigma_{w,\text{SPECULOOS-}E_{g'}}$ (ppm)	$\mathcal{L}(10^{-5}, 1000)$	$0.005^{+0.623}_{-0.005}$
$q_{1,\text{SPECULOOS-}E_{r'}}$	$\mathcal{U}(0, 1)$	$0.682^{+0.206}_{-0.268}$
$q_{2,\text{SPECULOOS-}E_{r'}}$	$\mathcal{U}(0, 1)$	$0.497^{+0.251}_{-0.251}$
Dilution factor, $D_{\text{SPECULOOS-}E_{r'}}$	$\mathcal{U}(0.5, 1)$	$0.896^{+0.063}_{-0.080}$
Offset relative flux, $M_{\text{SPECULOOS-}E_{r'}}$	$\mathcal{N}(0, 0.1)$	0.00008 ± 0.00005
Jitter, $\sigma_{w,\text{SPECULOOS-}E_{r'}}$ (ppm)	$\mathcal{L}(10^{-5}, 1000)$	$0.055^{+9.581}_{-0.054}$
$q_{1,\text{SPECULOOS-}G_{r'}}$	$\mathcal{U}(0, 1)$	$0.480^{+0.281}_{-0.273}$
$q_{2,\text{SPECULOOS-}G_{r'}}$	$\mathcal{U}(0, 1)$	$0.438^{+0.278}_{-0.274}$
Dilution factor, $D_{\text{SPECULOOS-}G_{r'}}$	$\mathcal{U}(0.5, 1)$	$0.667^{+0.143}_{-0.107}$
Offset relative flux, $M_{\text{SPECULOOS-}G_{r'}}$	$\mathcal{N}(0, 0.1)$	0.00023 ± 0.00019
Jitter, $\sigma_{w,\text{SPECULOOS-}G_{r'}}$ (ppm)	$\mathcal{L}(10^{-5}, 1000)$	$0.095^{+17.365}_{-0.095}$
$q_{1,\text{SPECULOOS-}I_{g'}}$	$\mathcal{U}(0, 1)$	$0.416^{+0.268}_{-0.243}$
$q_{2,\text{SPECULOOS-}I_{g'}}$	$\mathcal{U}(0, 1)$	$0.428^{+0.281}_{-0.262}$
Dilution factor, $D_{\text{SPECULOOS-}I_{g'}}$	$\mathcal{U}(0.5, 1)$	$0.813^{+0.117}_{-0.142}$
Offset relative flux, $M_{\text{SPECULOOS-}I_{g'}}$	$\mathcal{N}(0, 0.1)$	-0.00005 ± 0.00012
Jitter, $\sigma_{w,\text{SPECULOOS-}I_{g'}}$ (ppm)	$\mathcal{L}(10^{-5}, 1000)$	$0.057^{+5.620}_{-0.056}$
$q_{1,\text{SPECULOOS-}I_{r'}}$	$\mathcal{U}(0, 1)$	$0.594^{+0.227}_{-0.245}$
$q_{2,\text{SPECULOOS-}I_{r'}}$	$\mathcal{U}(0, 1)$	$0.545^{+0.243}_{-0.254}$
Dilution factor, $D_{\text{SPECULOOS-}I_{r'}}$	$\mathcal{U}(0.5, 1)$	$0.839^{+0.102}_{-0.115}$
Offset relative flux, $M_{\text{SPECULOOS-}I_{r'}}$	$\mathcal{N}(0, 0.1)$	0.00009 ± 0.00009
Jitter, $\sigma_{w,\text{SPECULOOS-}I_{r'}}$ (ppm)	$\mathcal{L}(10^{-5}, 1000)$	$0.563^{+36.628}_{-0.558}$
$q_{1,\text{SPECULOOS-}I_{z'}}$	$\mathcal{U}(0, 1)$	$0.587^{+0.239}_{-0.270}$
$q_{2,\text{SPECULOOS-}I_{z'}}$	$\mathcal{U}(0, 1)$	$0.520^{+0.246}_{-0.263}$
Dilution factor, $D_{\text{SPECULOOS-}I_{z'}}$	$\mathcal{U}(0.5, 1)$	$0.745^{+0.132}_{-0.129}$
Offset relative flux, $M_{\text{SPECULOOS-}I_{z'}}$	$\mathcal{N}(0, 0.1)$	0.00011 ± 0.00023
Jitter, $\sigma_{w,\text{SPECULOOS-}I_{z'}}$ (ppm)	$\mathcal{L}(10^{-5}, 1000)$	$0.319^{+6.179}_{-0.0317}$
NIRPS and HARPS RV parameters		
RV semi-amplitude, K_p (m/s)	$\mathcal{U}(0, 10)$	$4.324^{+1.036}_{-1.080}$
Relative systemic RV offset, μ_{NIRPS} (m/s)	$\mathcal{U}(0, 100)$	$1.672^{+1.712}_{-1.163}$
Jitter, $\sigma_{w,\text{NIRPS}}$ (m/s)	$\mathcal{U}(0, 10)$	$1.317^{+1.256}_{-0.975}$
GP amplitude, α_{NIRPS} (m/s)	$\mathcal{U}(0, 10)$	$3.568^{+0.529}_{-0.728}$
GP length scale, β_{NIRPS} (m/s)	$\mathcal{U}(1, 200)$	$89.935^{+61.742}_{-44.931}$
Relative systemic RV offset, μ_{HARPS} (m/s)	$\mathcal{U}(0, 100)$	$3.337^{+2.793}_{-1.921}$
Jitter, $\sigma_{w,\text{HARPS}}$ (m/s)	$\mathcal{U}(0, 100)$	$27.146^{+4.226}_{-3.523}$

Notes: $\mathcal{N}(\mu, \sigma)$ indicates a normal distribution with mean μ and variance σ^2 , $\mathcal{U}(a, b)$ a uniform distribution between a and b and $\mathcal{L}(a, b)$ a log-uniform distribution between a and b . The TESS sectors 12 (TESS-S12), 39 (TESS-S39) and 66 (TESS-S66) were modelled separate from each other. ExTrA-T1, ExTrA-T2, ExTrA-T3 refer to the three ExTrA telescopes. LCO-CTIO and LCO-SAAO are the two telescope part of the LCO network. SPECULOOS-south observed TOI-4552 using three of the four telescopes: Europa (SPECULOOS-E), Ganymede (SPECULOOS-G) and Io (SPECULOOS-I), with g' , r' and z' referring to the various

Sloan photometric filters. NIRPS and HARPS are the high-resolution spectrographs used for the velocimetry. The systemic RV offset for NIRPS is -25490.828 m/s and for HARPS is -25247.139 m/s. μ_{NIRPS} and μ_{HARPS} are relative to these values

Appendix C: TOI-4552 b interior structure modelling

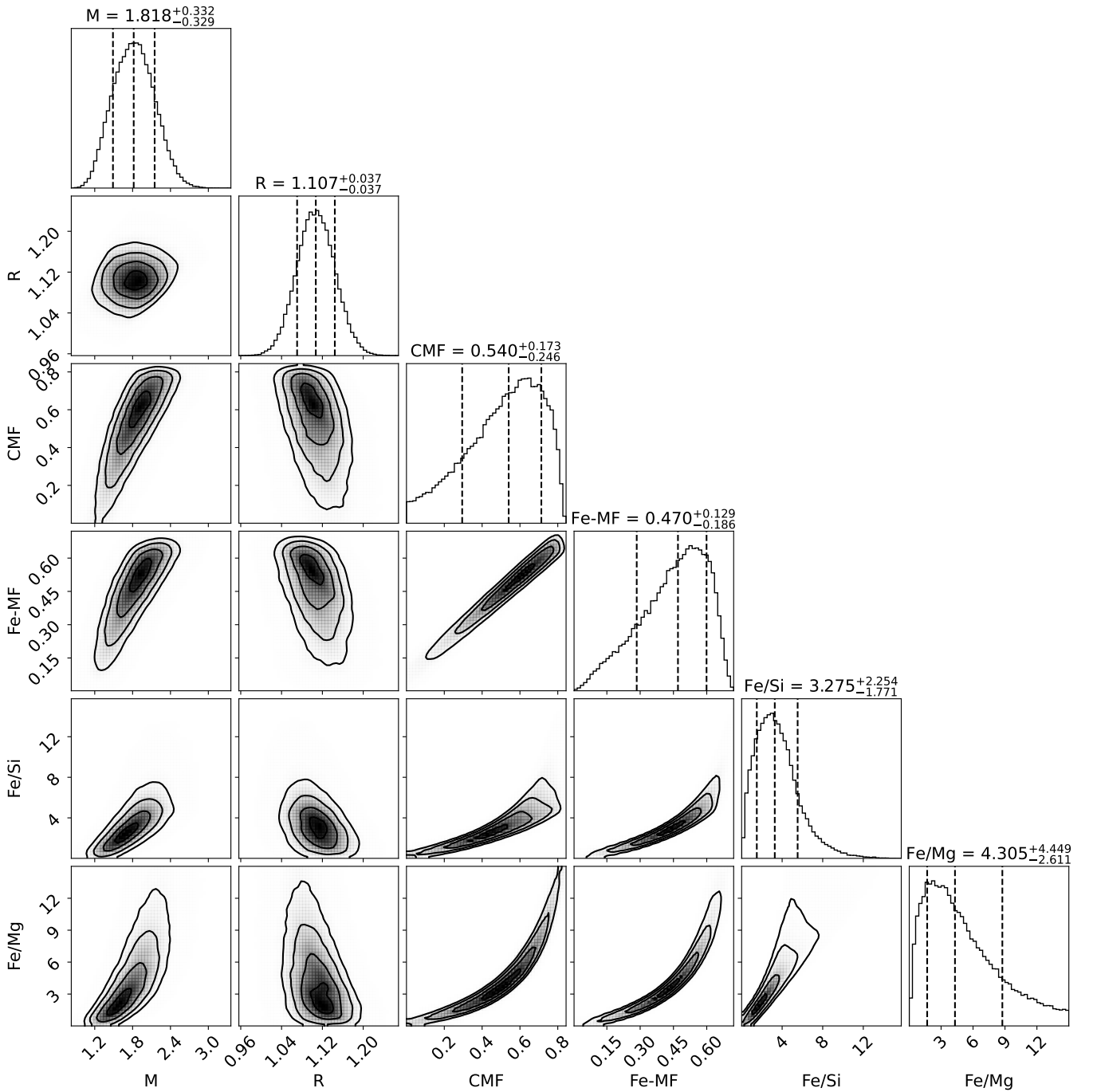


Fig. C.1: Corner plot depicting the interior structure model of TOI-4552 b using *exopie* (Plotnykov & Valencia 2024) with the planetary mass and radius as priors. The abundance of iron in the mantle and silicon in the core is left to vary freely between 0 and 20%. The resulting CMF of 0.54 is partway between that of Mercury ($=0.7$; Szurgot 2015) and Earth ($=0.33$), suggesting a marginal over-abundance of iron (also evident from the high iron mass fraction, Fe-MF).

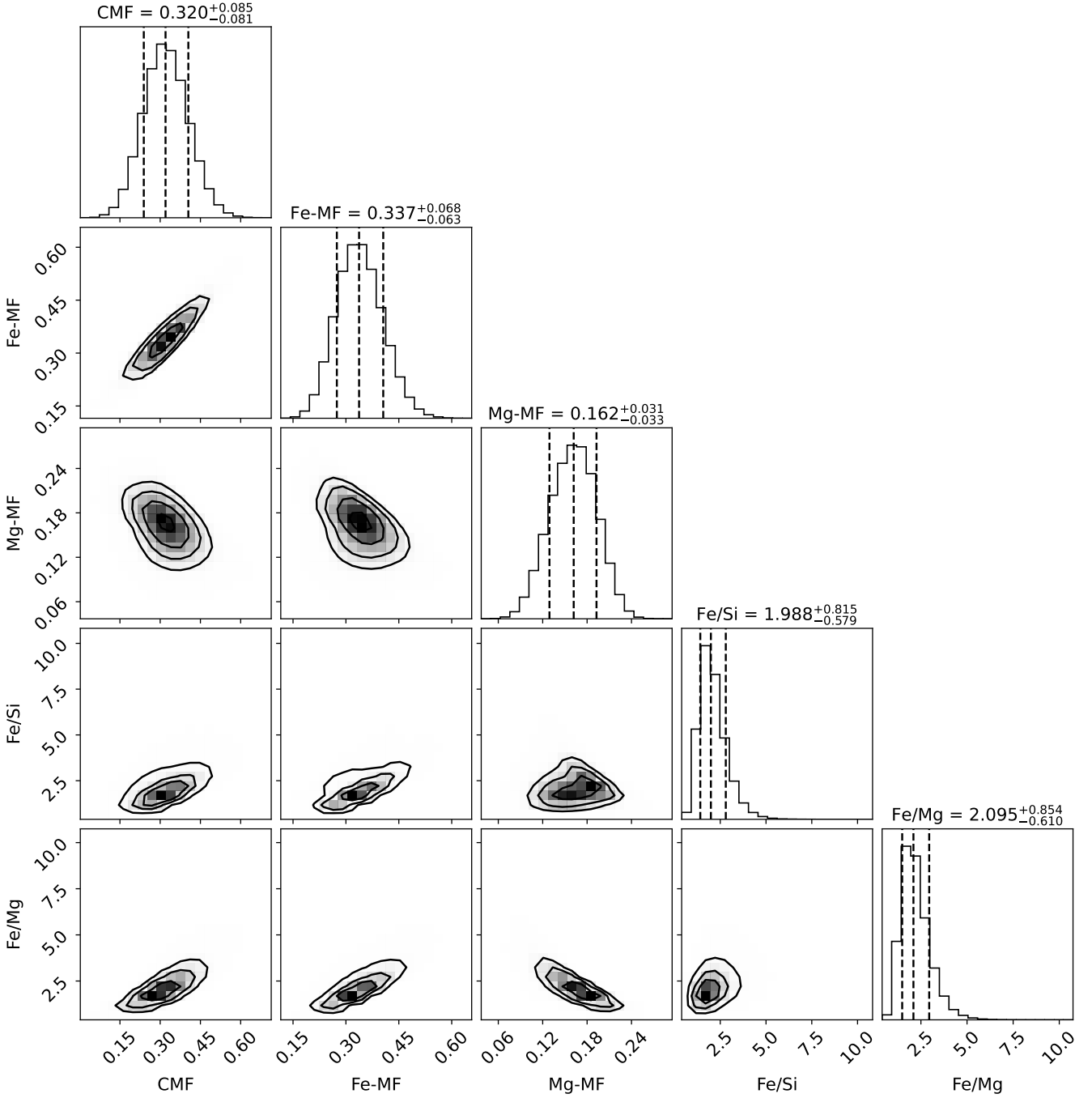


Fig. C.2: Corner plot of an alternative interior structure model illustrating the expected planetary properties under the assumption that the refractory element abundances of the planet match those of the host star. Therefore, only the stellar element abundances ($[\text{Fe}/\text{H}]$, $[\text{Mg}/\text{H}]$ and $[\text{Si}/\text{H}]$) were input as parameters, with $[\alpha/\text{H}]$ used as a proxy for $[\text{Mg}/\text{H}]$ and $[\text{Si}/\text{H}]$ due to very few lines used in the abundance measurements for those elements. No constraints were put on planetary mass and radius. The expected CMF for a rocky planet around TOI-4552 is 0.32, consistent with that of the Earth. This is just within the lower uncertainty bound predicted by the interior model constrained by the mass and radius measurements (CMF = $0.54^{+0.17}_{-0.25}$; Section 5.1; Fig C.1).